Master thesis
On

"Analysis of the Iranian Permanent GPS Network in the NE and E of Iran (time series and velocity field) and Modeling the stress transfer between active faults bounding the Lut block"

Supervision by:

Andrea Walpersdorf and Mathilde Vergnolle

Prepared by:

Amaneh Jadidi Mardkheh

Master Student of Erasmus Mundus program at
University of Joseph Fourier, Grenoble, France
Rose School, Pavia, Italy

2006-2007
Submitted on 31st of October 2007

Acknowledgement

I would like to thank very especially my advisors, Andrea Walpersdorf and Mathilde Vergnolle, for their support throughout my thesis. They helped me very kindly and provided me with the opportunity to explore lots of interesting paths.

I would also like to acknowledge the Director of Laboratoire de Geophysique Interne et de Tectonophysique, Grenoble, France, Fabrice Cotton, and his colleagues, and the Erasmus Mundus program who funded my study in Europe.

I thank Isabelle Manighetti for sharing her personal earthquake catalogue synthesis and her cartographic rupture plane map, and also for her helpful explanation on active tectonic setting of NE and E of Iran.

I would also like to express my gratitude to the Geodynamic department of National Cartographic Centre, Tehran, Iran, especially Mr Djamour, to provide the GPS data and information about them, and Mr Tavakoli for his useful comments.

I thank my parents and my fiancé Kyarash to provide me a comfortable environment and their help during this study.

For my family and my Love Kyarash
And all people in Iran

Outlines

1 Abstract

Iran is situated in a region of collision between two major tectonic plates, the Eurasian and the Arabian plates, with a convergence rate of 25±2 mmyr-1. The historical earthquakes that occurred before the 20th century and recorded data clearly show that Iran has always been shaken by largely destructive earthquakes. This study is concentrated on the northern and eastern part of Iran.

In the first part of this study we present a combined solution of the permanent Iranian GPS network (65 stations) and campaign GPS networks. We established a combination solution with a global IGS network and compare this method with SOPAC solutions and a solution limited to the regional network. We explore the effect of the new atmospheric modelling (concerning atmospheric loading and mapping functions) in particular on the height component. We defined an optimal reference frame for our studies in Iran with 36 stations distributed densely over the whole world. We investigate the contribution of the permanent stations to improve the reference frame of campaign networks and their coordinate estimation. We explore the compatibility of permanent site velocities with close by campaign sites on bedrock. In this study, we recognized that the combination solution (regional networks and global IGS network) is the best strategy to obtain more precise coordinates with respect to the ITRF2000 reference frame. We detect that the mapping function VMF1 and the modelling of atmospheric loading improve significantly the height component. We give evidence for the use of permanent stations improving the campaign reference frames. We observed periodical subsidence of 20 cm/yr at the TOUS station and 6 cm/yr at the NISH station which are located in NE Iran close to Mashhad.

In the second part of this study, we examine 3 past large earthquakes that occurred in the NE of the Lut block, in NE Iran, to understand whether these disaster earthquakes changed the proximity of failure of the surrounding faults. The first destructive one occurred on the 31st of August 1968 (Mw 7.1). The next one occurred on the 27th of November 1979 (Mw 7.1). It is the largest event of a series of 48 events in 1979. These two M>7 earthquakes broke the East West left lateral Dasht-e-Bayaz fault system. Finally, the last disaster happened on the 10th of May 1997 and broke the north part of the SN right lateral Abiz fault system. The tendency of the rocks to fail in a brittle manner is thought to be a function of both shear and normal stresses, commonly formulated as the Coulomb failure criterion (King et al, 1994). In this study, based on the variation of the Coulomb stress failure hypothesis, we explore the possible stress triggering relationship between these three large earthquakes. We also investigate the relationship between each large earthquake with their aftershocks and evaluate the Coulomb stress variation on the surrounding faults. So we release the two large earthquakes in 1968 and 1979 were a major criterion to make advance the earthquake on Abiz fault in 1997. And also these 3 large earthquakes are activated a large kilometre area on Lut block. The variation of stating Coulomb stress changes is between 0.02-5 bars on the southern part of the Abiz fault on Sistan suture as increasing stress and has dropped by the same value on most part of area. The seismicity is high after the 1997 earthquake, and located not only in the areas that have their potential to break increased. We thus think that the earthquakes that occurred in the shadow stress areas result from another process than the static Coulomb stress perturbation caused by the preceding 3 large earthquakes and needs more consideration.

2 Introduction

2.1 Tectonic settings of Iran

Iran is situated in the Himalayan and Alpine seismicity belt. It is located between the Arabian and the Eurasian plates (Figure1). Iran is accommodating deformation resulting from the convergence of the two plates. The total shortening in the Iran area has been predicted to be between 28 and 40 mm/yr at 60°E. The large uncertainty results from the ambiguities in the interpretation of see floor spreading data in the Red Sea and the Aden Gulf (Walker et al., 2004; Demets et al., 1994; Jestin et al., 1994; Chu & Gordon, 1998). According to published GPS results, the present-day shortening between Arabia and Eurasia is 25 mm/yr at 60° E (Vernant et al., 2004).

About a third to a half of the Arabia-Eurasia convergence (10-12 mm/yr) is taken up in the central Zagros (Tatar et al., 2002), so that 13-15 mm/yr of shortening at 60°E remains to be accommodated further north, in central Iran, the Alborz mountains and by the South Caspian Basin. This amount of shortening should result in an equal amount of N-S right lateral shear in eastern Iran, with respect to the Hellmand block east of Iran being part of the Eurasian plate (Walker et al, 2004). The right lateral shear, south of 34°N, is accommodated on N-S right lateral strike-slip faults to the east and west of the Lut desert. In the north of the Lut desert, the dominant structures are the Doruneh and Dasht-e-Bayaz left-lateral strike-slip faults, which are thought to accommodate right-lateral shear by clockwise rotation away from the direction of the maximum shortening (Jackson & McKenzie 1984; Jackson 1995). The same rotations have been proposed for strike-slip faults in eastern Tibet (England & Molnar, 1990; Holt et al., 1991).

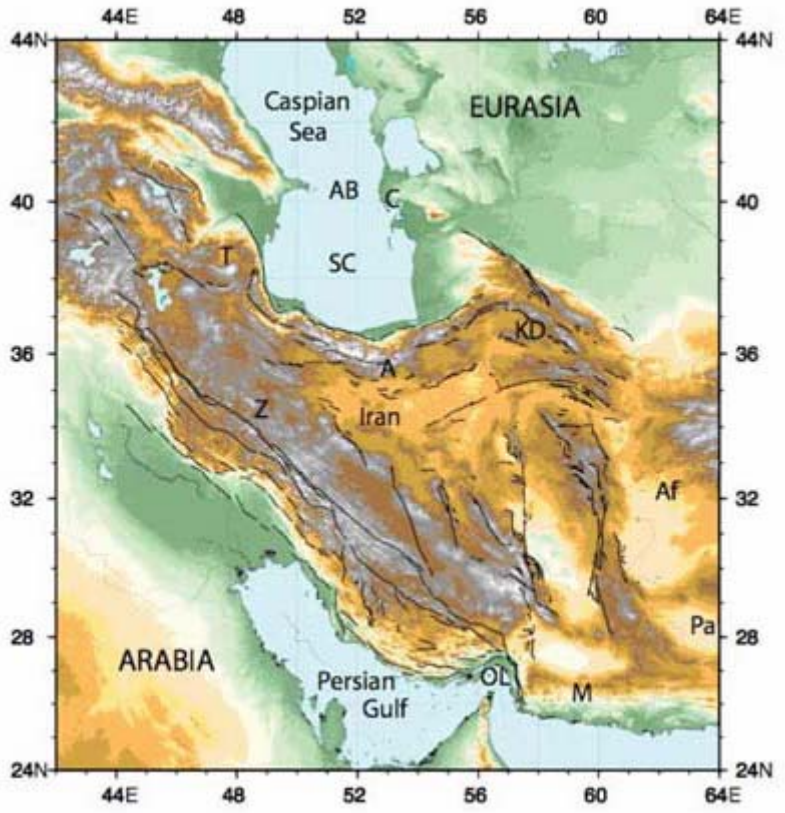

Figure 1 : Topographic and active fault map of Iran and surrounding regions. Geographic and tectonic features indicated are: Afghanistan (Af); Pakistan (Pa); Apscheron–Balkhan sill (AB); Cheleken (C); South Caspian basin (SC); Talesh mountains (T); Alborz mountains (A); Kopeh Dagh (KD); Zagros

Mountains (Z); Oman Line (OL) and Makran (M). The compilation of faults is courtesy of Richard Walker.

Since many years, Quaternary stratigraphy and geomorphological methods are employed in Iran to establish cartography of active faults. This task is difficult because of the thick sedimentary layer covering large parts of Iran which leads to the existence of blind faults (basement faults not reaching the surface). Other active faults are difficult to identify because they are creeping aseismically and are not related to seismicity (Hessami et al., 2003). Because of the high density of active faults, some of the earthquake sources cannot be associated with a single fault. The lack of accurate, complete fault maps results in the inability to correlate seismic data with the active faulting in the region. .

Eastern Iran is characterized by upper crustal seismicity surrounding the aseismic Lut block which is accommodating at its eastern and western limits the N-S right lateral shear between central Iran and Afghanistan of around 10-16 mm yr^{-1} (Figure 2).This shear is absorbed mostly by N-S trending strike-slip faults on the eastern and western side of the Lut block. In its northern part shear is taken up by E-W trending left lateral strike-slip faults (Doruneh, Dasht-e-Bayaz) that rotate clockwise. Shear eventually ends as shortening against the Turkmenistan platform in the Kopet-Dagh range of NE Iran (Figure 2). South of the Lut block is the shoreline of the Oman Sea with the Makran subduction zone. The subduction is related to weak mantle seismicity. Most of the shortening between the Indian Ocean plate and the Hellmand block (Afghanistan) is accommodated by the Makran subduction zone (19 mm/yr, Vernant et al., 2004).

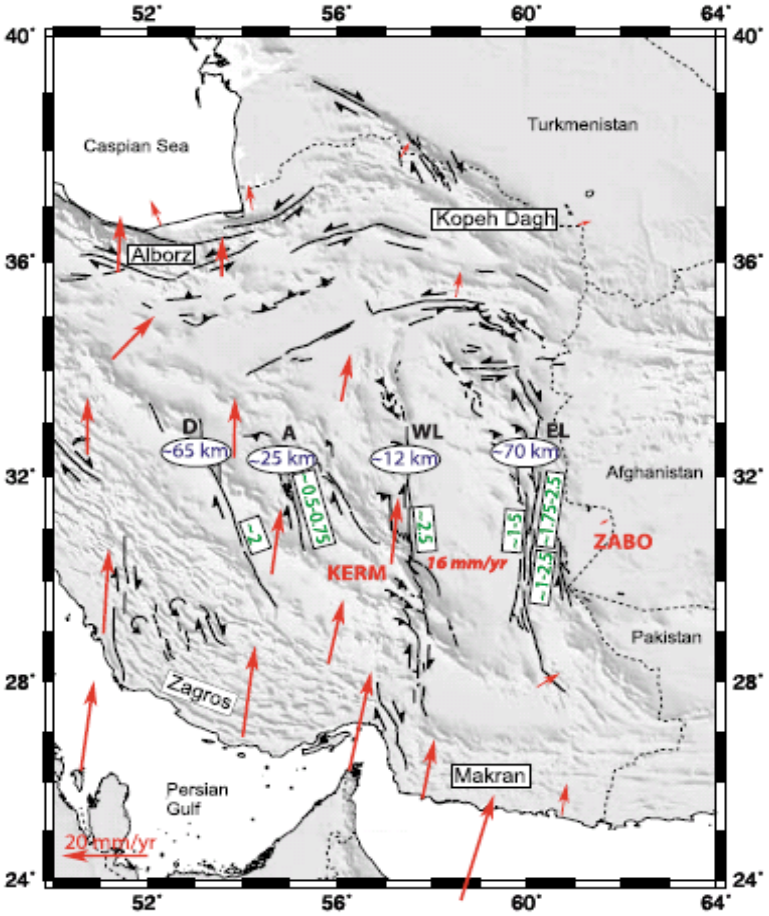

Figure 2 : Strike-slip faulting in Central and Eastern Iran. Modified after Walker and Jackson [2004]. Total offsets across Dehshir (D), Anar (A), West Lut (WL), and East Lut (EL) faults are indicated in km. GPS velocities relative to stable Eurasia (red arrows, Vernant et al., 2004) indicate ~16 mm/yr of right-lateral shear across WL and EL fault systems. Slip-rate on individual faults (green numbers in mm/yr) is

averaged over the Quaternary for West Lut (Walker and Jackson, 2002) and the Holocene for Deshir (Meyer et al., 2006), Anar and East Lut (Meyer et al., 2007)

The active tectonics related to the Arabia-Eurasia collision in Iran induces a high seismicity localized in different Iranian regions. The seismicity is distributed in the high mountain ranges in the south and north of the country, respectively in the Zagros Mountain and in the Alborz and Kopet Dagh mountains (Figure 3). It is also localized on the faults bounding the aseismic blocks such as the Central Iranian block or the Lut block (Figure 3). About one earthquake of M>7 occurs every 7 years and about one earthquake of 6<M<7 occurs every 2 years since 1900 in the whole Iranian area (Ambraseys and Melvile, 2005). This high seismicity in Iran is a crucial problem for the population because each large earthquake induces a lot of damage and casualties. The number of injured and dead people is indicated on the USGS web site http://earthquake.usgs.gov/regional/world/historical_country_mag.php#iran. A better understanding of the seismic risk and potential related to the major faults and fault systems in Iran is a substantial task for the Iranian population.

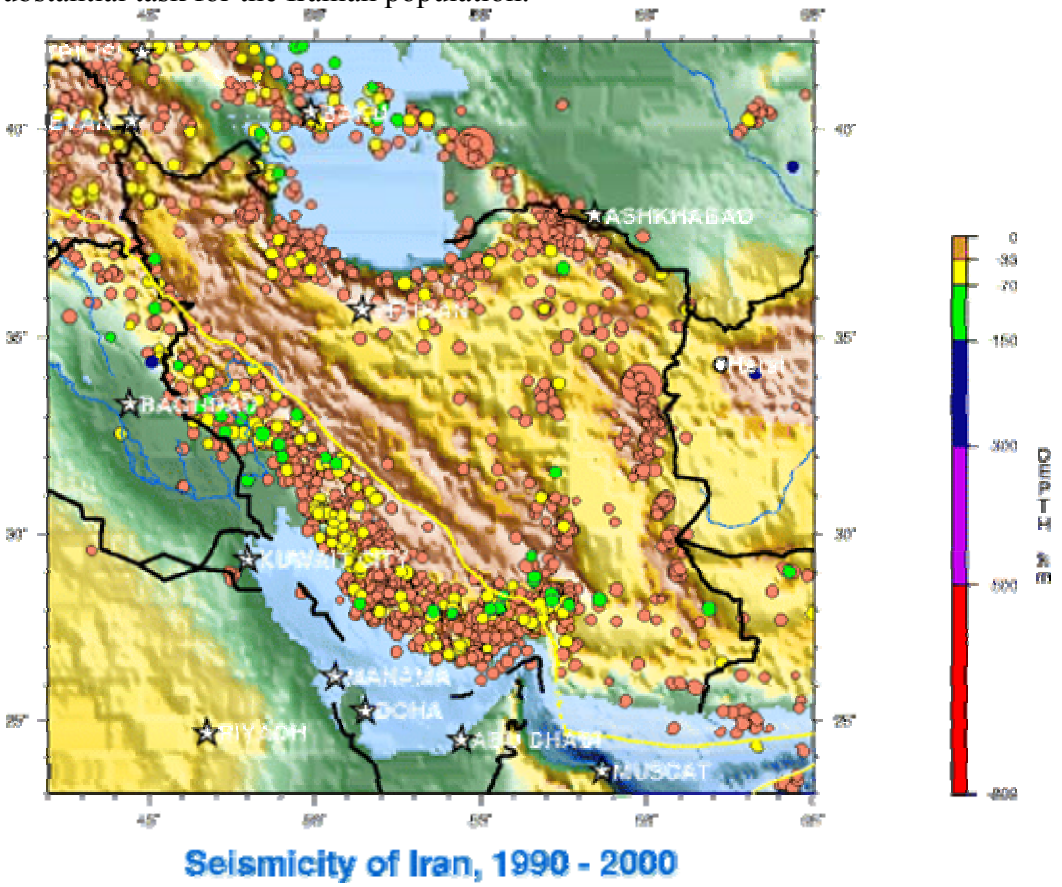

Figure 3 : Seismicity of Iran from 1990 to 2000 according to the USGS catalogue

2.2 Geodetic measurements of present day kinematics in Iran

The tectonic context and the resulting seismic risk identify Iran as an important natural laboratory for the study of the dynamics and kinematics of the Earth's crust. A first important step to understand Iran's present-day tectonics is to monitor the crustal deformation precisely by geodetic measurements such as VLBI, SLR, INSAR and GPS. The GPS measuring method has several advantages over the other techniques, for example the ability to collect data continuously, the lower costs of GPS instruments which are also more

compact and easier to handle. The present GPS receiver technology and scientific software enable us now to obtain precise results in positioning and station displacement, making GPS a powerful tool for geodynamic applications.

The National Cartographic Center of Iran (NCC), with collaboration of French scientists, has established since 1997 several GPS campaign networks in the most important Iranian regions according to seismicity and population density (e.g. the Iran Global network presented in Figure 2). To increase information on present-day crustal deformation and fault activities used for estimating seismic hazard, the National Cartographic Center has established since 2005 a GPS permanent network which consists of 107 stations distributed according to two strategies. 1) A part of the station covers in a regular way the whole of the Iranian country. 2) Another part of the stations are dedicated to monitor closely active faults in highly populated areas. This network has to be managed and processed as carefully as possible to get as soon as possible significant results concerning the position and velocity of each station. This information is highly awaited to help characterizing the seismic hazard in the different Iranian regions. While the campaign stations are mostly measured for a few days every two years, the continuous data from the permanent stations permit to position them once every 24 hours. This increases the positioning precision of the permanent stations with respect to campaign stations and allows better constraining of the station velocities after about two years of measurement. However, for safety reasons, the Iranian permanent stations are often installed close to habited areas on soft ground, while temporary stations are installed on outcrops of bedrock. Therefore, permanent stations could show displacements due to local phenomena (hydrology, gravity, monument instability, etc …) and not only due to the activity of the tectonic units they represent.

2.3 Objectives of the GPS data processing implemented in this study

The data of the Iranian permanent stations are analyzed in this Master thesis for several aims: One is to produce first significant results from the data of the new Iranian permanent network and to identify the best strategy for establishing the reference frame for the Iranian permanent network. Another is to test the compatibility of permanent site velocities with close by campaign sites on bedrock. A third aim is to test whether the reference frame of the campaign measurements can be improved by the combination with the analysis of the permanent network. For these purposes, we have chosen very carefully our processing strategy and we have conducted several methodological tests. In the beginning of this research work, we hoped to be able to process the permanent network from the date of installation in 2005 up to mid 2007. Over a two-year's time span, the accuracy of the velocity field should be reasonably well constrained. However, only data until mid 2006 have been available. This limited data set does not permit to infer significant tectonic velocities. Nevertheless, methodological studies have been performed and an analysis strategy has been defined which is ready for an optimal data processing of the full data set as soon as these data arrive. Precise questions we want to study are:

- What are the first significant results from the data of the new Iranian permanent network?
- What is the best strategy for establishing the reference frame for the Iranian permanent network?
- Are the permanent site velocities compatible with close by campaign sites on bedrock?
- Can the reference frame of the campaign measurements be improved by the combination with the analysis of the permanent network?

- Can the campaign solutions be improved by new, up to date analysis strategy?

2.4 Fault interaction and earthquake clustering in Iran

In Iran, the historical seismicity catalogue clearly shows that earthquakes occurred in clusters on several fault systems (Figure 2) as the Neh fault (east boundary of the Lut block), the Sabzevaran fault, the Gowk and Nayband fault system (west boundary of the Lut block), or the Dasht-e-Bayaz and Abiz fault system (north boundary of the Lut block). The sequence of earthquakes can be more or less complex. On the Nayband fault for example the sequence occurred on a segmented fault whereas on the Dasht-e-Bayaz and Abiz fault system, they occurred on different faults that intersect themselves (Figure 2). A lot of questions arise from this clustering of earthquakes. Among them: What is the organization of the earthquakes on the different faults? Does the sequence of earthquakes always happen at each earthquake cycle or does it happen occasionally? How a large earthquake on a fault affects the surrounding faults? Is there a relationship between the earthquakes of the same sequence? What are the stress transfers between the earthquakes? Is the stress transfer between earthquakes significantly higher than the regional tectonic loading?

To try to reply to some of these questions, we propose to study the stress transfer interaction between the earthquakes that occurred in the NE of the Lut block on the Dasht-e-Bayaz and Abiz fault system. Three large events of magnitude higher than 7.1 occurred in 1968, 1979 and 1997 and 48 events of magnitude $4<M_w<7.1$ occurred in this period. Our objective is to understand whether these disaster earthquakes changed the proximity of failure on the Lut Block and whether the earthquakes in this series may have been triggered by the preceding one(s). We based our analysis on the Coulomb stress failure criterion and calculated the static Coulomb stress change between the successive earthquakes (King et al., 1994). According to King et al., (1994) and Stein et al. (1999), Coulomb stress change hypothesis can explain the succession of earthquakes and the distribution of aftershocks. When an earthquake happens, it produces a net reduction of regional stress in the proximity of its rupture but also a stress increase elsewhere (depending on the mechanism of faulting). Some studies (e.g. King et al., 2003) suggest that immediately following a large event, the rate of seismicity increases in the region where overall stress field has been elevated and the rate of seiemicity decreases regions where the stress field has been reduced (stress shadow). Then, this criterion, if valid, allows one to predict if one earthquake could advance or delay a second earthquake on the prolongation of the first rupture or in its surrounding area and to predict area where one can expect an increase number of earthquakes following a main shock. In this study we investigate if the static Coulomb stress change caused by the major earthquakes could explain the occurrence of the next large earthquake and the distribution of the seismicity in our studied area. We then use the Coulomb stress calculation to estimate how the potential to failure along the Dasht-e-Bayaz and Abiz faults, and associated faults have been affected by the three major events. We propose to use our results to determine the faults where earthquakes would be advanced or delayed in the future in this region.

2.5 Objectives of Coulomb stress transfer modeling implemented in this study

In this study, we can not reply to the wide range of questions that cluster of earthquakes arise (see section 2.4) but we will try to reply to the following questions:

- How the three large earthquakes of the Dasht-e-Bayaz and Abiz fault system affect the surrounding faults?
- Is there a relationship between these three earthquakes?

- Does the stress transfer between these earthquakes increase their probability of occurrence?
- Is the stress transfer between earthquakes is significantly higher than the regional tectonic loading?
- How long does recurrence time of large earthquake is affected by stress transfer?

Part I

3 GPS processing and results

3.1 Iranian Permanent GPS Network (IPGN)

The complete coverage of the Iranian territory for monitoring crustal deformation, fault activity and co- and post-seismic deformation would need one station every 30 km. As the Iranian area is 1650000 km², to cover densely this whole area, it needs to establish at least one station in each 900 km² cell. That means 1800 stations are needed, but installing and running this huge number of stations takes time and a lot of money. Therefore, choices for the establishment of the Iranian permanent GPS network had to be done. Up to present, there are 107 stations in the IPGN. They are split up in four dense regional networks with 25-100 km spacing between the stations, and one large scale network (200-500 km spacing) to estimate the general tectonic deformation of Iran covering the Alborz Mountains in the north, the Zagros Mountains in the south, and the east and west of Iran. The most important criteria to decide about the station distribution can be mentioned as: Historical earthquake locations, highly populated areas, high seismic hazard and highly active faults. Figure 4 presents the distribution of IPGN stations.

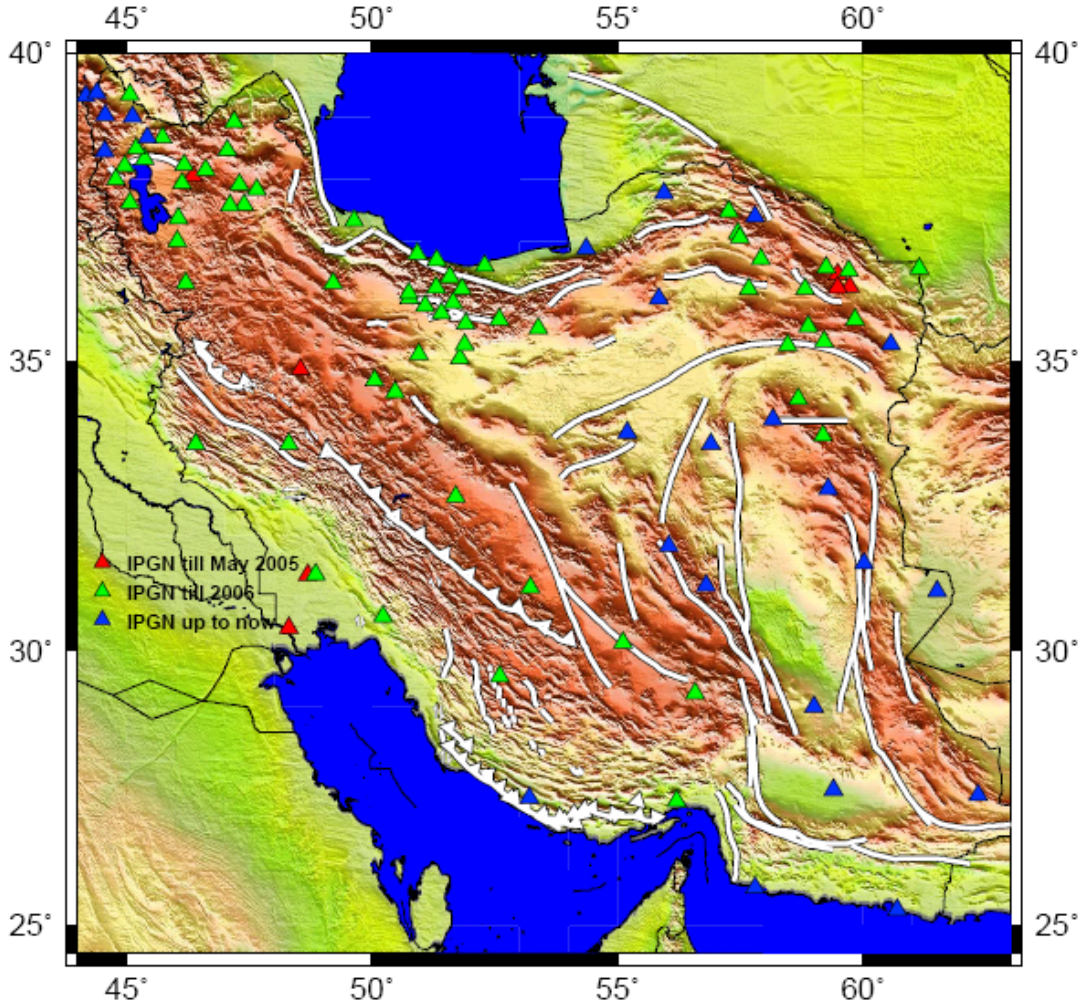

Figure 4 : Distribution of the Iranian Permanent GPS network; classified by different colours with respect to the monument date of permanent stations .

Each permanent station is equipped with a GPS receiver, a communication device (telephone or GSM modem) and a back up battery. The GPS antenna is fixed on top of a concrete pillar and the receiver and the other equipment are installed in the rack closed to the pillar which is shown on the Figure 5.

Figure 5: Pillar and rack of HSGD station

3.1.1 Tehran and central Alborz network (29 stations)

The Alborz mountain belt is a zone of high seismic activity (Figure 3). Tehran as the capital of Iran with a population of more than 12 million and many economic, social, cultural and industrial facilities is located in the southern mountain foots of central Alborz. The 29 stations of the Tehran/central Alborz network (Figure 6) are distributed 25-30 km from each other, up to now all of the stations are operational and are analyzed on a regular basis.

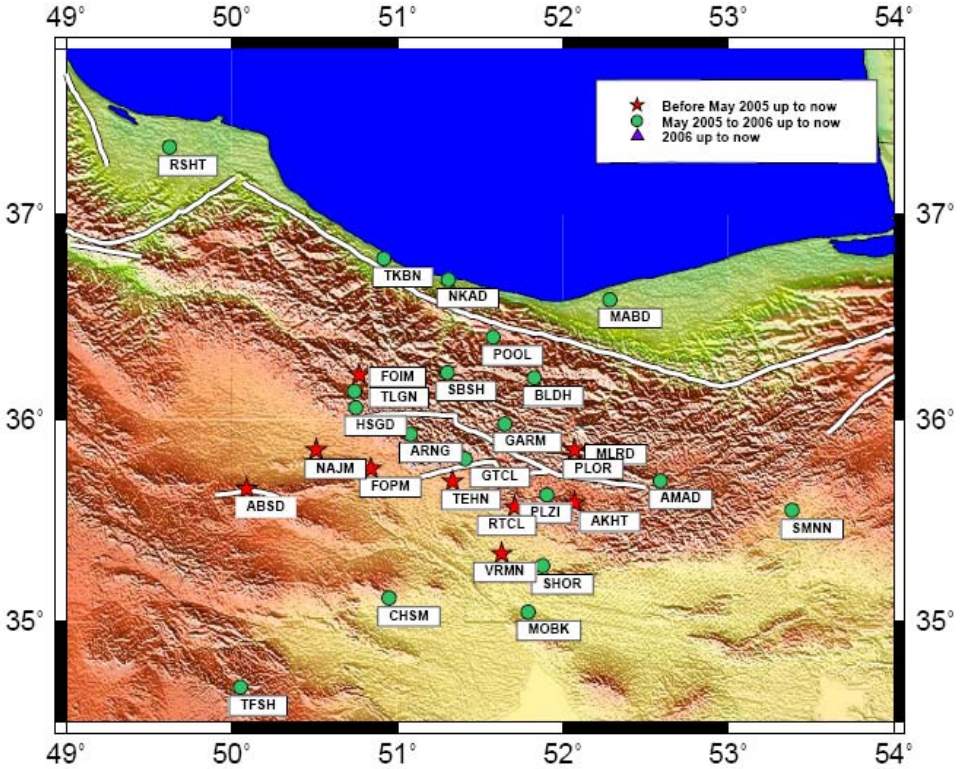

Figure 6: Distribution of the GPS stations of the Tehran/central Alborz network.

3.1.2 Tabriz network (25 stations)

In the north-western Iranian regions of Azerbaijan and Ardabil, there are many active faults such as the Tabriz, Tassouj and Baladan faults. The Tabriz fault is one of Iran's most active faults with a GPS observed velocity of 7 mm/yr. 25 stations have been planned to be established in this region (Figure 7).

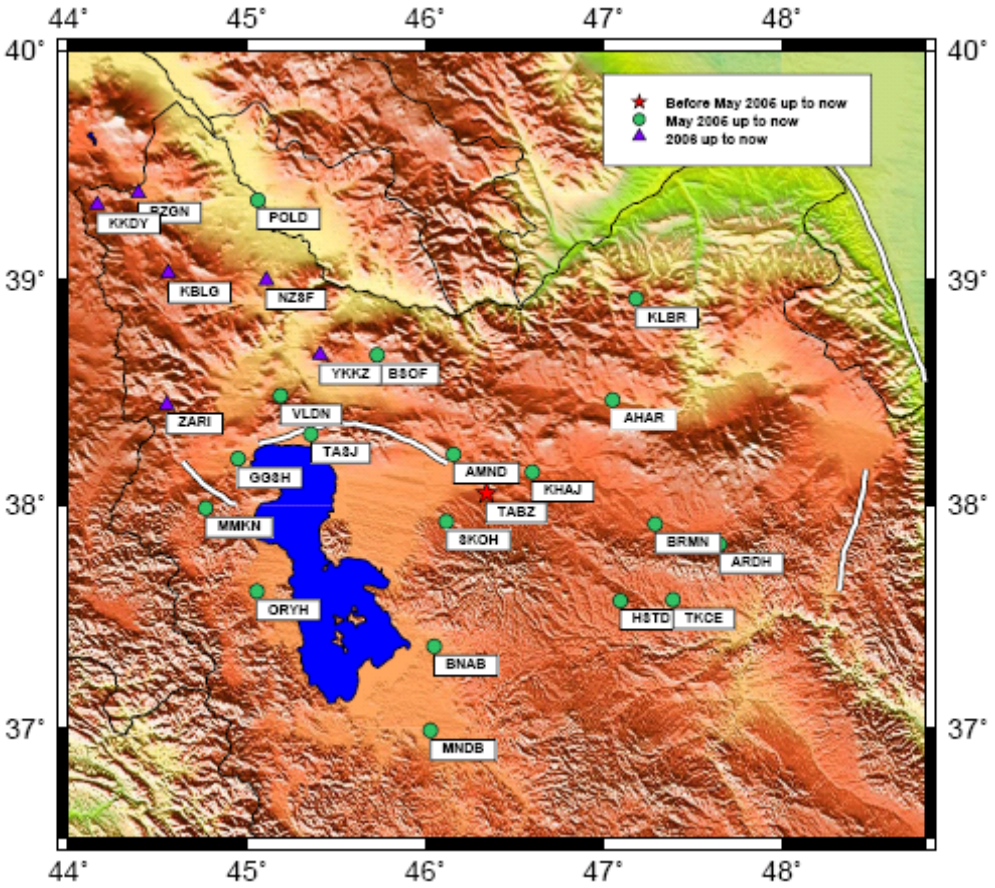

Figure 7: Distribution of GPS stations in the Tabriz network in NW Iran.

3.1.3 Khorasan network (29 stations)

Mashhad, Neishaboor, and Sabz-e-var are the major cities in the highly populated Khorasan region in NE Iran. This region has historically been shaken by several disastrous earthquakes which destroyed the whole area and killed most of the population. To observe the tectonic deformation and infer constraints on the seismic loading of the active faults in this region, 29 stations have been installed (Figure 8).

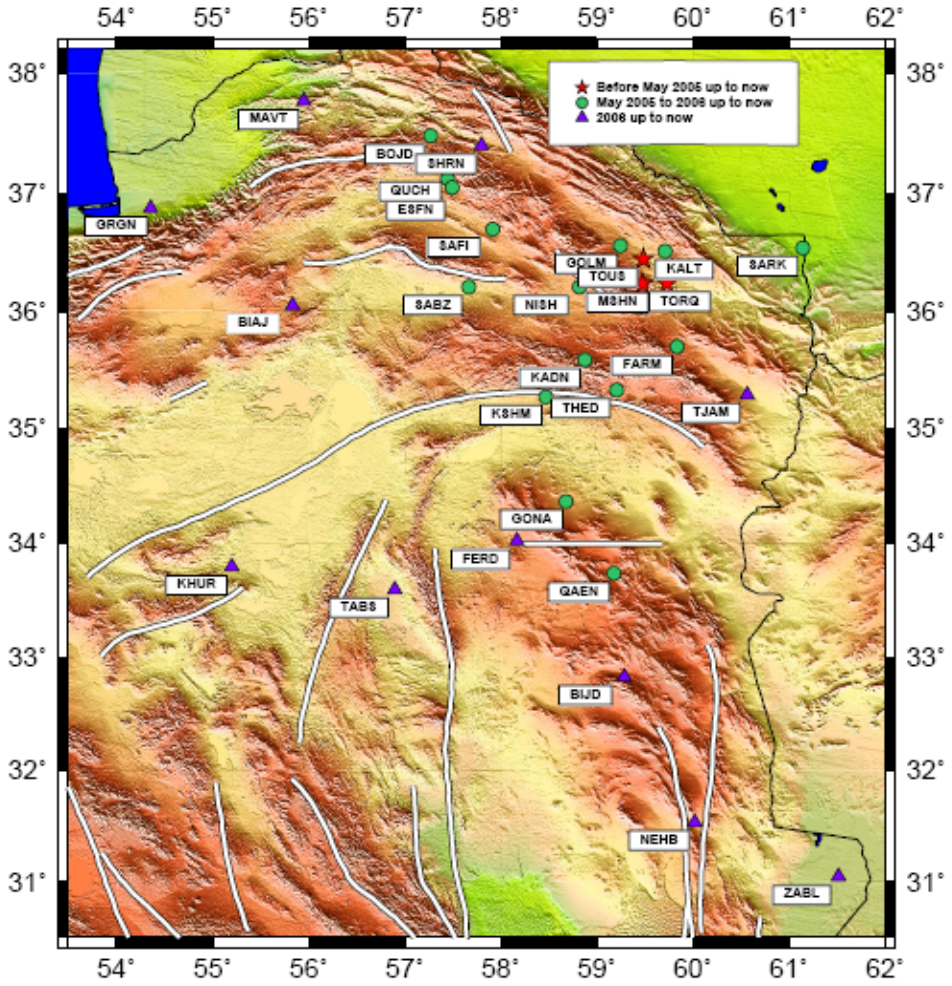

Figure 8 : Distribution of the GPS stations of the Khorasan Network in NE and E of Iran

3.1.4 Ahvaz network (18 stations) and Hamedan network (6stations)

Many active faults are found in the western, southern and central Iran which is however a less populated area. In this case, 18 stations have been established in the area of the Zagros and the Makran (Ahvaz network) shown on Figure 9. Six other stations of the Hamedan network cover the western part of Iran (including the west part of Zagros, Figure 10).

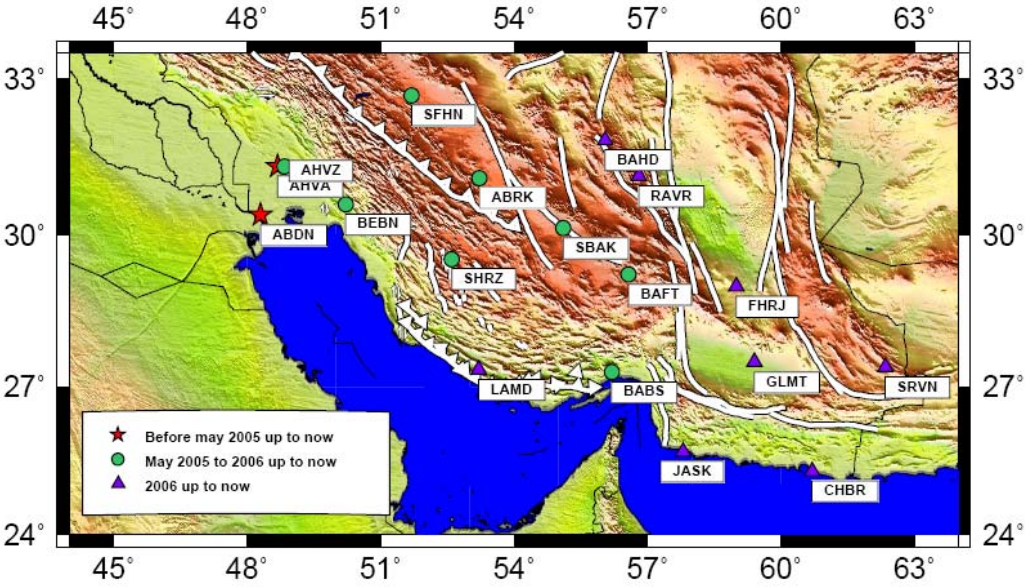

Figure 9 : Distribution of stations of the Ahvaz network in the SW and S of Iran

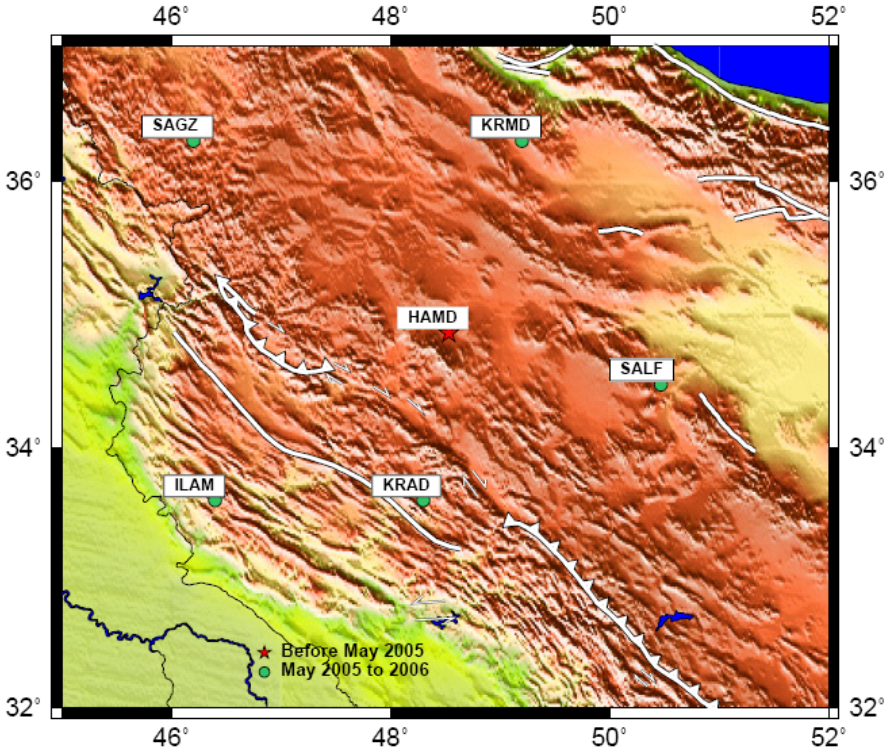

Figure 10: Distribution of the stations of the Hamedan network in the western part of Iran

3.2 Campaign networks

As shown on Figure 11, several campaign networks were installed in most of the active regions in Iran and observed for at least 48 h once every 2 years. The total observation span is mainly 5 to 6 years to obtain at least 3 measurements on each station. The total time span and the number of measurements are dependent on the displacement rates expected in the network.

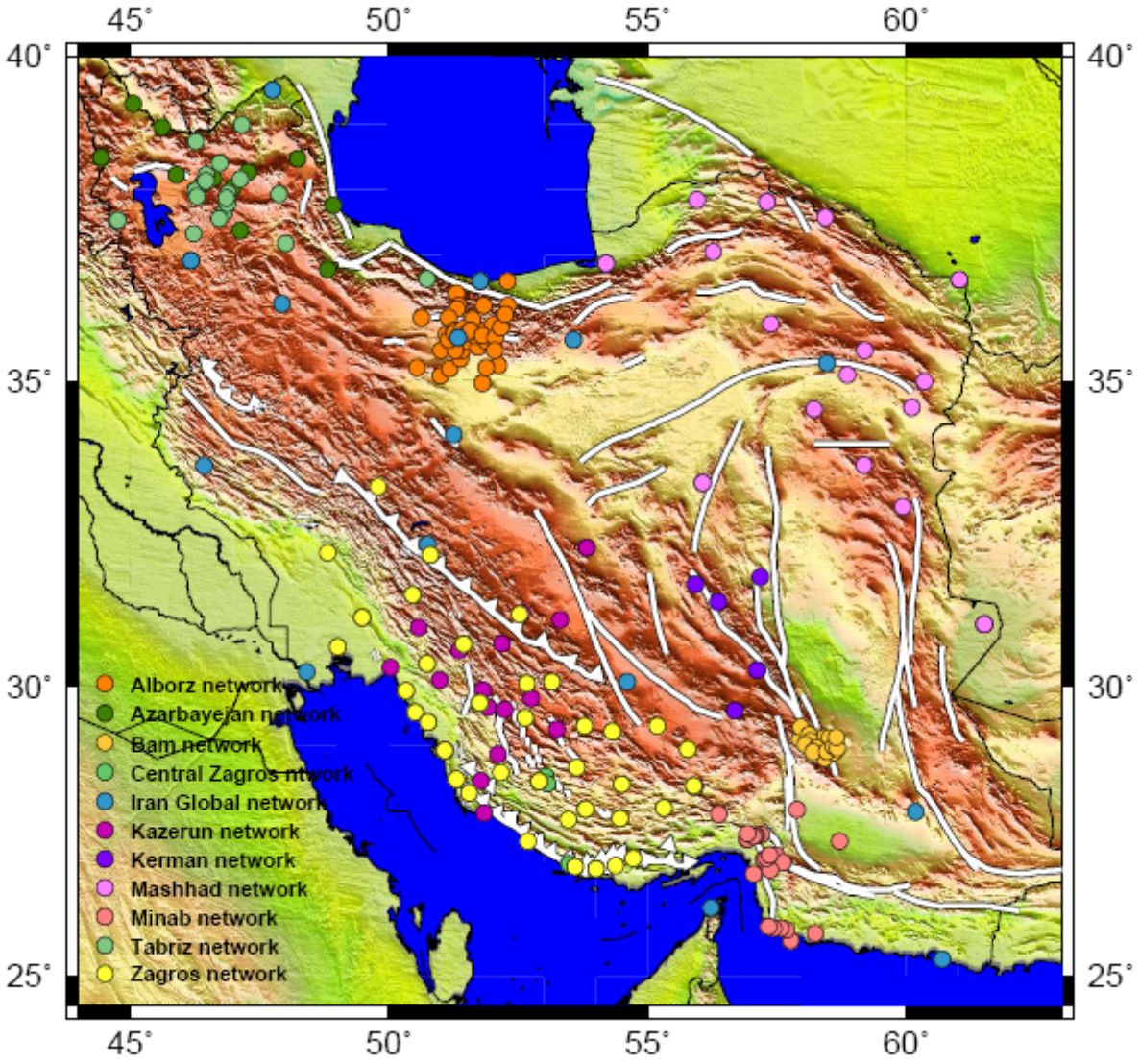

Figure 11 : Distribution of campaign networks; classified by different colours with respect to the each individual campaign networks

Three measurements over 5-6 years can usually resolve velocities to better than 2 mm/yr. The campaign networks are regional networks and relatively dense. They are supposed to measure all identified active faults in the observation zone by at least one station to each side of the faults. To obtain the total fault velocity with two sites per fault the stations must be located at least 20 km far from the active fault trace, to be outside a deformation zone created by the locking of the fault. Most of the stations are established as screw markers fixed in bedrock outcrops to reduce set up errors by forced antenna centering. Some stations are concrete pillars with forced centering of a tribrach, and the rest of them are standard bold marks to be measured with tripods and tribrachs. The GPS stations used for the campaign measurements are Trimble 4000SSI, Ashtech XII and Ashtech microZ receivers. All receivers were combined with chock ring antennas. The complete list of campaigns network measurements done in Iran is:

- Alborz network
- Tabriz network
- Bam post-seismic network: 4 measurements from 2004-2006.
- Central Zagros network: The first Iranian network started in 1997 and re-measured in 2000 and 2003.
- Iran Global network: Observed in 1999, 2001 and 2005.

- Kazerun network: Observed 2002, 2004, and 2006.
- Kerman network: Observed in 2004, and 2006. Tow more measurement campaigns are necessary to resolve the slow differential velocities in this network (< 2 mm/yr).
- Mashhad network: A first set of stations has been measured in 2004 and 2006. Densification stations have been measured in 2005 and 2007. Re-measurements are needed to resolve the slow differential velocities (< 2 mm/yr)
- Minab network
- North Zagros network: Observed in 2001, 2003 and 2005.

3.3 Methodology

In order to achieve significant results of velocities and strain rates for geodynamic purposes, we take to account the station age of permanent stations (at least two years), and the number of repeat measurements of campaign networks (at least 3 epochs). Two epochs would be enough to infer a site velocity, but systematic errors cannot be detected by only two measurements. So for geodynamic aims you have to choose campaigns with confirmed site velocities from at least three measurements. According to these criteria, we processed 50 stations, with half of them distributed over the whole country and half of them concentrated in the eastern and north-eastern part of Iran from 2001 to August 2007. This network is designed to monitor precisely the tectonic deformation in E and NE Iran, in a highly precise reference frame established over the whole country. To obtain significant observations of tectonic deformations in this region, one main criterion to choose stations was the age of the stations. Therefore, we classify the permanent network into three sub-networks, stations operational before May 2005 (which should have more than two years of data in a final processing done in August 2007), stations operational between May 2005 and beginning of 2006, and stations from the begining of 2006 up to now. These sub-networks are shown on Figures 4 and 6-10 in each regional sub-network. In addition to the permanent data, we included some of the campaign networks in the NE, E and S part of the country: The Central Zagros network, the Kazerun network, the North Zagros network, the Kerman network and the Mashhad network. All data used in this study were collected by NCC (the permanent data) or in collaboration of NCC with LGIT (the included campaign data).

The data are analyzed in daily sessions. For each day of the analysis, observation files in compressed Receiver Independent Exchange (RINEX) format with data in a 30 second interval are used. Supplementary data required to analyze the Iranian GPS measurement are GPS data from global reference stations from the IGS network (International GNSS Service), broadcast navigation files and a priori orbits (IGS final solutions). These data were downloaded from the SOPAC or CDDIS archive for each day. All files were collected on a day by day basis just prior to subsequent processing of each daily solution, as described in following text.

The daily site coordinates were estimated from the GPS measurement using the scientific software packages GAMIT version 10.32 (King and Bock 2007) and then combined to global campaign solutions or multi-epoch velocity solutions by GLOBK, version 5.12 (Herring, 2007).

For stabilization of our regional network and for connection to a global reference frame we include IGS stations in the processing of the Iranian Permanent GPS Network. In our case we consider two IGS networks. The first one is a big global network of about 55 stations covering the entire world in a regular way (about equally spaced). These stations are chosen from the IGS core list (the ensemble of IGS stations used to determine GPS satellite orbits). The main selection criteria are:

- Performance (no none-tectonically offsets)

- Monumentation date (at least 2 years before 2000)
- Continuity (no gap in the data observation from 2000- up to now)
- Geographical distribution (equally spaced network).

The second IGS network is a smaller network consisting of IGS stations located close to Iran, especially on the Eurasian plate and the Arabian plate surrounding the Iranian collision zone. The stations of the smaller, local IGS network are also part of the IGS core stations and common with the large, global network. Figure 12 shows the distribution of stations from both IGS network. The global IGS network stations are:
ASC1, ARTU, BAHR, BJFS, BRAZ, CAS1, CHAT, COCO, CRO1, DGAR, FLIN, GRAS, GLPS, GUAM, HOFN, IISC, IRKT, JOZE, KARR, KELLY, KERG, KOKB, LHAZ, MANA, MAC1, MALI, MAS1, MAS1, MAW1, MDO1, NAMA, NICO, NKLG, NAY1, PERT, PETP, PIMO, POL2, QUIN, RAMO, RIOG, SANT, STJO, SUTH, TEHN, THTI, TIXI, TOW2, TRAB, TRO1, TSKB, VILL, UNSA, USNO, WHIT, WTZR.

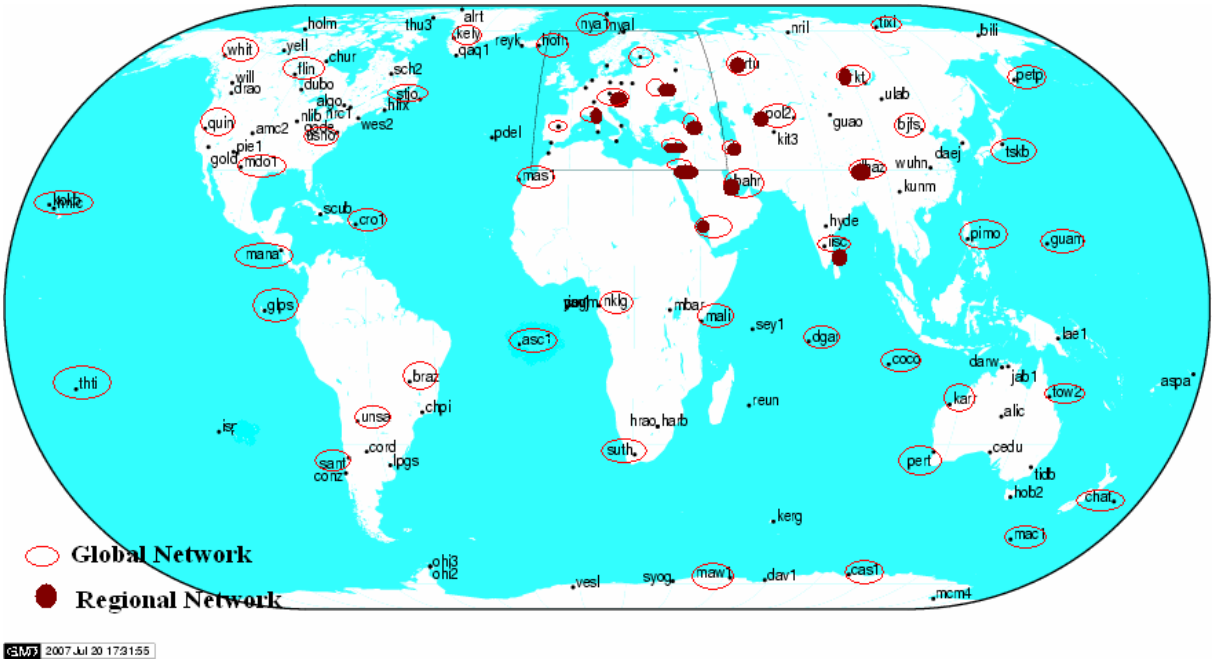

Figure 12: Distribution of IGS stations of both the regional (bold red circle) and the global network (red circle) analyzed in this study.

The local IGS network stations are:
ARTU, BAHR, GRAS, JOZE, IISC, IRKT, LHAZ, NAMA, NICO, POL2, RAMO, TEHN, TRAB, WTZR.

The IPGN consists nowadays of 107 stations. We have selected 63 permanent stations for our analysis (selecting the oldest stations of the IGPN). The GAMIT processing is limited to a maximum of 55 sites in a single solution. This is a reasonable limit optimized for present-day CPU power and RAM capacity. The procedure to analyze bigger networks consists in forming sub-networks with some overlapping stations and combining the solutions at a later step of the analysis, in the global solution performed by the Kalman filter GLOBK. The best strategy to choose sub-networks has been identified in Jadidi et al. (2006) as the following:

- Analyze a global network of IGS stations independently with the same strategy applied to the regional networks (55 stations are globally covered the world), this avoids including solution of global IGS network published by SOPAC but analyzed with different strategies.

- Analyze 10-15 regional IGS stations together with most of the Khorasan network stations and some stations of the Tehran network stations (a total of 28 stations) and, when available, 10-15 stations from campaign networks. (Figure 13 yellow box)
- Analyze 10-15 regional IGS stations together with the Tabriz network, the Ahvaz network (Zagros and Lut block) (a total of 32 stations) and, when available, 10-15 stations from campaign network. (Figure 13 pink box)
- Notice that there are some common regional stations of the IPGN in both sub-networks to establish the link between the independent daily coordinate estimations when they are combined by the Kalman filter. These stations are indicated in Table1 and 2.

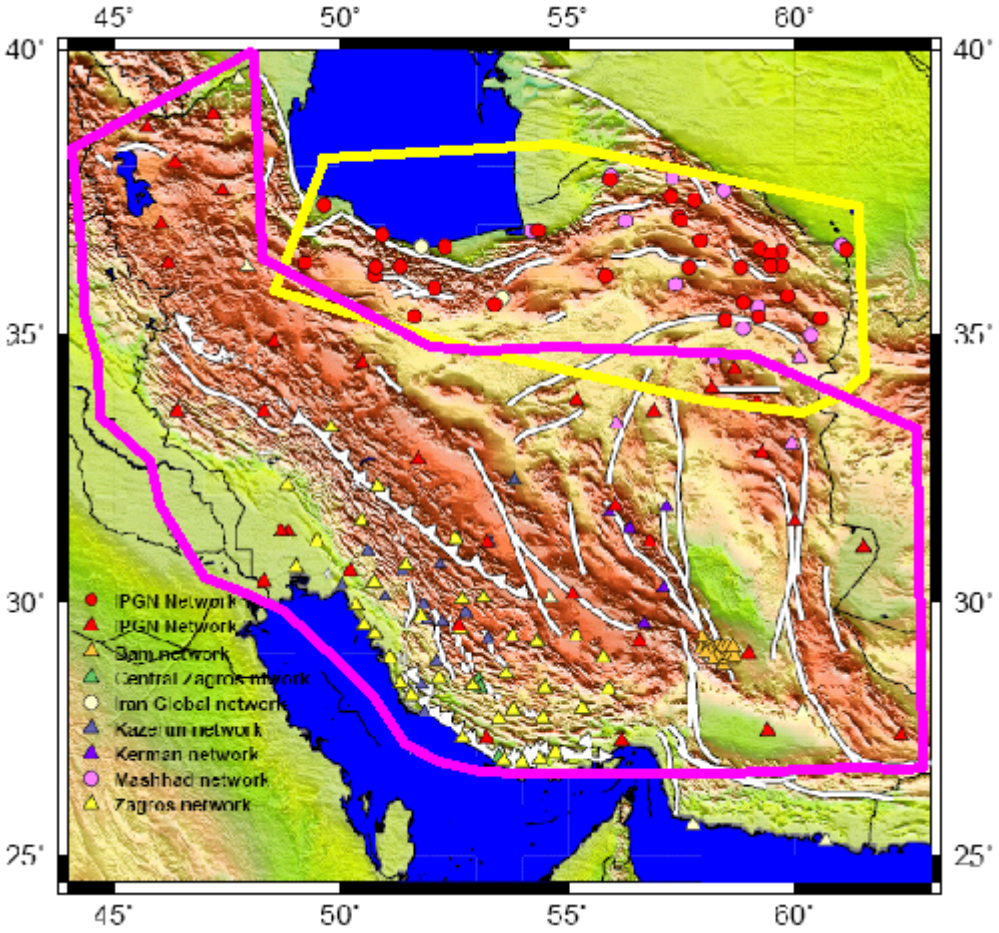

Figure 13 : Distribution of the two regional sub-networks analyzed in this study, classified with different colours with respect to the monumentation date for permanent stations and different campaigns networks; yellow box: sub-network 1, pink box: sub-network2

The stations list of Network1						
The situation of Tehran Network stations						
	Station Id	St. Name	Latitude	Longitude	Start time	Percentile of existence
1	TEHN	NCC	35.697	51.334	01.12.1999	100%
2	FOIM	Imam Airport	36.180	50.770	18.04.2005	100%
3	HSGD	Hashtgerd	36.060	50.750	07.04.2005	100%
4	MABD	Mahmood abad	36.588	52.285	07.08.2005	100%
5	PLOR	Plour	35.850	52.070	28.09.2006	100%
6	RSHT	Rasht	37.327	49.624	02.11.2005	100%
7	SBSH	Siahbishe	36.231	51.303	15.05.2005	90%

8	SMNN	Semnan	35.553	53.387	17.05.2005	100%
9	TKBN	Tonekabon	36.788	50.919	17.08.2005	100%
10	VRMN	Varamin	35.340	51.630	15.04.2005	100%
The situation of Khorasan Network stations						
11	BOJD	Bojnourd	37.480	57.270	04.07.2005	100%
12	FARM	Farmahin	35.700	59.840	31.05.2005	100%
13	KADN	Kadkan	35.590	58.880	12.06.2005	100%
14	KALT	Kalat rod	36.511	59.713	19.06.2005	100%
15	KSHM	Kashmar	35.270	58.470	11.09.2005	100%
16	GOLM	Golmakan	36.560	59.250	30.11.2005	100%
17	MSHN	Mashhad	36.235	59.480	22.12.2002	100%
18	NISH	Nishabour	36.210	58.820	24.05.2005	100%
19	QUCH	Qouchan	37.120	57.450	13.06.2005	100%
20	SABZ	Sabz-e-var	36.210	57.670	14.12.2005	100%
21	SARK	Sarakhs	36.540	61.150	15.09.2005	100%
22	SHRN	Shirvan	37.400	57.800	03.05.2005	100%
23	THED	Torbat-e-Heydarieh	35.330	59.210	18.05.2005	100%
24	TORQ	Toroq	36.240	59.730	22.04.2005	100%
25	TOUS	Tous	36.445	59.489	24.12.2004	100%
26	GRGN	Gorgan	36.876	54.354	06.02.2006	100%
27	BIAJ	Biarjmand	36.053	55.834	27.03.2006	100%
28	MAVT	Marveh Hill	37.770	55.950	13.08.2006	100%
29	SAFI	Safi Abad	36.698	57.921	26.06.2005	-----
30	ESFN	Esferayen	37.049	57.495	19.07.2005	-----
31	TJAM	Torbat-e-Jam	35.290	60.570	19.08.2006	-----
Hamedan Network						
32	KRMD	Khoramdareh	36.3	49.2	21.05.2005	100%

Table 1: List of stations which are included the regional network1. Common stations of with regional network 2 are marked by red colours.

The stations list of Network2						
The situation of the Tabriz Network stations						
	Station Id	St. Name	Latitude	Longitude	Start time	Percentile of existence
1	BSOF	Babereh-e-Sofla	38.670	45.730	01.10.2005	100%
2	KLBR	Kalayber	38.918	47.181	16.07.2005	100%
3	MNDB	Myandoab	36.990	46.030	17.12.2005	100%
4	TABZ	Tabriz	38.056	46.343	16.12.2003	100%
5	TKCE	Torkemanchay	37.580	47.390	09.07.2005	100%
The situation of Ahvaz Network stations						
6	AHVA	Ahvaz	31.340	48.684	09.02.2001	70%
7	ABDN	Abadan	30.4	48.3	30.01.2005	30%
8	AHVZ	Meterological Institue	31.343	48.844	07.06.2005	100%
9	ABRK	Abarkouh	31.120	53.227	09.08.2005	100%
10	BABS	Banadar-e-Abbas	27.3	56.2	26.10.2005	60%
11	BAFT	Baft	29.239	56.580	23.06.2005	100%
12	BEBN	Behbahan	30.605	50.216	16.11.2005	60%
13	SBAK	Shar-e-Babak	30.14	55.10	05.07.2005	60%
14	SHRZ	Shiraz	29.54	52.60	20.11.2005	100%
15	SFHN	Esfehan	32.7	51.7	26.11.2005	85%
16	BAHD	Bahabad	31.84	56.04	23.07.2006	-----
17	LAMD	Lamard	27.35	53.2	19.07.2006	-----
18	RAVR	Ravar	31.15	56.80	14.05.2006	-----

19	FHRJ	Fahraj	29	59	06.09.2006	-----
20	SRVN	Saravan	27.40	62.35	13.11.2006	-----
21	GLMT	Golmoorti	27.5	59.4	21.09.2006	-----
The situation of Khorasan Network stations						
22	GONA	Gonabad	34.37	58.68	04.07.2005	100%
23	QAEN	Qaen	33.74	59.18	03.10.2005	100%
24	BIJD	Birjand	32.83	59.29	10.01.2006	100%
25	FERD	Ferdous	34.02	58.16	07.03.2006	100%
26	KHUR	Khour	33.80	55.20	14.08.2006	-----
27	NEHB	Nehbandan	31.53	60.02	24.08.2006	-----
28	TABS	Tabas	33.60	56.90	13.08.2006	-----
29	ZABL	Zabol	31.04	61.51	28.09.2006	-----
The situation of Hamedan Network stations						
30	HAMD	Hamedan	34.86	48.53	21.01.2004	100%
31	SAGZ	Saqez	36.30	46.20	10.05.2005	100%
32	KRAD	Khoram abad	33.60	48.30	28.06.2005	100%
33	ILLM	Ilam	33.6	46.4	03.07.2005	100%
34	SALF	Salafchegan	34.48	50.47	31.07.2005	100%

Table 2: List of stations that are included in regional network 2. Common stations of with regional network 1 are marked by red colours.

3.3.1 Daily Solution

Double-differenced, ionosphere-free linear combinations of the L1and L2 phase observations were used to generate weighted least square solutions for each day of the analysis interval. An automatic cleaning algorithm (LC_AUTCLN) was applied to post-fit residuals to repair cycle slips and detect challenging data. Data cleaning was performed on 30 second data. These data were then decimated to a 4 minutes rate for the final least squares solution. IGS final orbit solutions are introduced as a priori values in each daily solution (*.sp3 files). Estimated parameters for each daily solution include the three dimensional Cartesian coordinate for each site, 6 orbital elements for each satellite (semi-major axis eccentricity, inclination, longitude of ascending node, argument of perigee, and Mean anomaly), Earth orientation parameters (pole position and rate UT1 rate), and integer phase ambiguities. We also estimated piecewise-linear atmospheric zenith delays at each station over two hour intervals to correct for the poorly modelled troposphere. Moreover, one east-west and one north-south horizontal tropospheric gradient has been estimated per day to account for tropospheric azimuthal asymmetry. The elevation cut off angle 0° was assigned and the absolute IGS antenna models (IGS_05) were used for the effective phase centre of the receiver and satellite antennas. Also pole tide and ocean loading models are included in the processing. Furthermore, we modelled atmospheric pressure loading with the ATML files provided at MIT to take into account elastic deformation of the earth crust caused by atmospheric pressure loading. This improves in particular the analysis of sites close to the equator on all three components and the accuracy of the height component of sites situated elsewhere (Tregoning and van Dam, 2005). We applied the Vienna Mapping Function (VMF1) which is developed by Boehm et al. (2006) to modify coefficients of the extended fraction in the mapping function that are derived by ray-tracing through actual meteorological data (ECMWF analyses updated every 6 hours) rather than by using best-fitting values from climatology's of radiosonde data or just parameters describing a standard atmosphere.

3.3.2 Reference Frame definition

Investigating crustal deformation for geodynamic purposes requires a global reference frame to which measurements from different locations and different times can be uniquely referenced. Therefore, a terrestrial reference frame which rotates with the Earth's surface is well-suited. The fundamental terrestrial reference frame preferred for all modern geodetic studies is called the International Terrestrial Reference Frame (ITRF). The orientation of the Cartesian axes is such that the z-axes coincide with the mean pole of rotation for the period 1900-1905, and the x-axes are in the plane of the Greenwich meridian. The rotation rate has a no-net-rotation condition for the horizontal motions with respect to the lithosphere. We employed ITRF2000 to characterize our stations. ITRF2000 was released in March 2001, resolved by 51 stations shown on Figure 13. The details of ITRF definition can be found at http://itrf.ensg.ign.fr .

The particular set of stations used to define the global reference frame was selected to provide optimal global stability over our processing interval. We have tested several sets of reference stations and checked the residuals between our fit to ITRF and the original ITRF solution. As result, we excluded some of the stations with less good fits to ITRF from the stabilization process: GRAS, JOZE, DGAR, KOKB, MANA, NYA1, PETP, RAMA, TEHN, ASC1, CRO1, NAMA, MKEA, QUIN, PETP and PIMO. The remaining stations are shown on Figure 14 by green symbols.

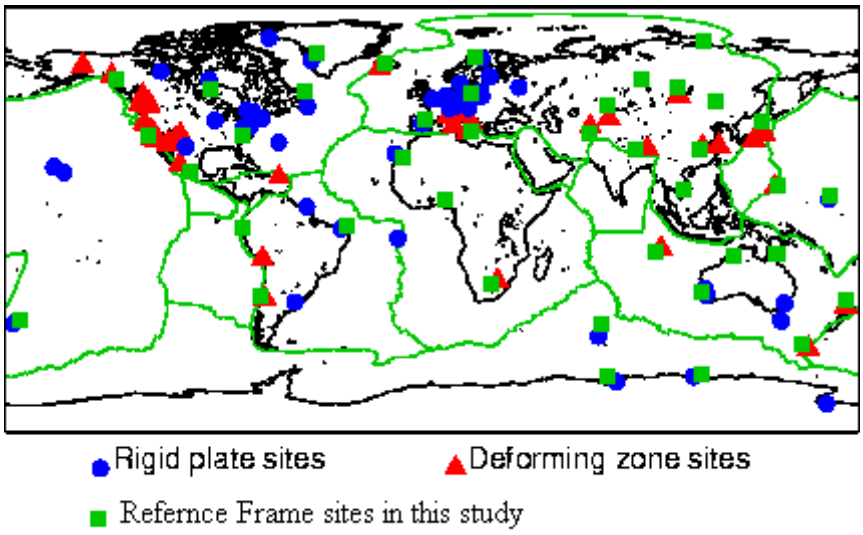

Figure 14 : The 51 IGS stations used to define ITRF2000 (red and blue symbols). Green symbols indicate the stations are used to define the ITRF reference frame in this study.

3.3.3 Combination of Daily Solution (Time-series and Velocity field)

To establish time series of station coordinates, in a first step, the unconstrained solution parameters from individual GAMIT solutions from the same day (e.g. the two Iranian sub-networks and the global IGS network) were input as pseudo-observations to the GLOBK Kalman filter for combination into single daily unconstrained solutions (Dong et al, 1998, Herring 2000). Reference frame constraints were then applied to each daily solution by Helmert transformation rules. For each day, 7 free parameters (3 translations, 3 rotations, and scale) were estimated by:

$$\begin{bmatrix} N \\ E \\ U \end{bmatrix} = \begin{bmatrix} -\sin(\lambda)\cos(\phi) & -\sin(\lambda)\sin(\phi) & \cos(\lambda) \\ -\sin(\phi) & \cos(\phi) & 0 \\ \cos(\lambda)\cos(\phi) & \cos(\lambda)\sin(\phi) & \sin(\lambda) \end{bmatrix} \begin{bmatrix} X \\ Y \\ Z \end{bmatrix} \quad (1.1)$$

NEU and XYZ are daily position of each site in the topocentric coordinate system and Cartesian coordinate system respectively. They uncertainty of this calculation defines with weighted least mean square and normalized least mean squat as:

$$wrms = \sqrt{\frac{\frac{n}{n-2}\sum_{i=1}^{n}\frac{(x_i - (y(t_i))^2}{\sigma_i^2}}{\sum_{i=1}^{n}\frac{1}{\sigma_i^2}}} \quad (1.2)$$

Where $y(t_i)$ is the observed 3D motion (see below), x_i is the estimated value of the three components, n is number of measurements, and σ_i is standard deviation value on each component.

Time-series resulted from daily combined solutions by applying a forward Kalman filter and a backward smoothing filter. We filtered white noise, and random walk noise to clean data, corresponding to Zhang et al (1996) to get realistic result. The reference frame to combine the orbit solutions was realized by tightly constraining the IGS stations to their values in the global reference frame ITRF2000.

The IGS sites were constrained according to the $1-\sigma$ position errors, which are site dependent, but approximately 2 mm (N), 2mm (E) and 5 mm (U). Mathematically, the observed motion of each site in the three directions (NEU) which is plotted by time-series can be expressed as:

$$y(t_i) = a + bt_i + c\sin(2\pi t_i) + d\cos(2\pi t_i) e\sin(4\pi t_i) + f\cos(4\pi t_i) + \sum_{j=1}^{n_g} g_j H(t_i - T_{gj}) + v_i + ... \quad (1.3)$$

Where t_i for i=1….N are daily solution epochs, H is Heaviside step function. The first two terms are site position, a, and linear rate b. coefficient c and d describe annual periodic motion, while e and f represent semi-annual motion. The remaining term corrects any number of offsets (n_g) with magnitude g at epoch T_g. v_i is associated to the white noise scenario. In this study we assumed walk random noise that can be added after the white noise terms.

As same generalized system can be applied to estimate a consistent set of coordinates and velocities for each site from daily combined solutions which contain the site coordinates, orbits and EOPs and their covariance matrix. To stabilize our solution with respect to the stable plate of Eurasia, we performed several tests. In the first test, we use the plate definition tools of the GLOBK software. This tool permits to define the Eurasian reference frame by minimizing the horizontal velocities of identified stations on the Eurasian plate and determining an Euler pole of the Eurasian plate with respect to ITRF2000. We used 6 IGS stations which are located on the Eurasian plate (Table 3). The resid ual velocities of these stations with respect to a rigid plate rotating with the Euler pole which has been estimated are around 0.5 mm yr^{-1}.

Then we followed Vernant et al. (2004) and used their Euler pole definition (Lat (°N): 56.11±1.4; Lon (°E): -100.79±1.9; Rate (°Myr^{-1}): 0.26±0.01) to define the Eurasian reference frame. We obtained differences of about 1 mm yr^{-1} when comparing the results corresponding to our own Euler pole with those obtained using Vernant et al. (2004).

Eurasian and Central Asian sites used to define Eurasian fixed reference frame							
Site	Lon.(°E)	Lat. (°N)	Vel_E (mm/yr)	σ_E (mm/yr)	Vel_N(mm/yr)	σ_N (mm/yr)	RHO
VILL_GPS	356.048	40.444	-0.25	0.36	-0.24	0.18	0.012
TIXI_GPS	128.866	71.634	0.45	0.18	0.46	0.29	0.009
IRKT_GPS	104.316	52.219	-0.11	0.17	-0.11	0.24	-0.003
ARTU_GPS	58.560	56.430	-0.03	0.19	-0.03	0.17	-0.015
TRO1_GPS	18.940	69.663	-0.53	0.64	-0.53	0.41	0.000
WTZR_GPS	12.879	49.144	0.08	0.26	0.08	0.16	0.005
Rotation pole of Eurasia in ITRF2000							
Plate	Lon(°E)		Lat(°N)		Rate(°M/yr)		
Eurasian	-98.383±2.812		50.753±0.914		0.25±0.005		

Table 3: The Eurasian frame is determined following the approach of McClousky et al (2000). It is minimized the adjustment to the horizontal velocities of the 6 stations on the Eurasian plate.

3.4 Results and Discussion

In the beginning of this study we hoped that we were able to process all available data of the IGPN from 2001 up to now. Unfortunately we could not obtain timely the data after day of year 155 in 2006. Therefore, this calculation is based on processing of permanent data from 2001 to 155 in 2006. We could not obtain significant velocities in the east part of Iran from the IPGN because most of the stations have been monumented in mid 2005 and 2006. The data span of one year is too short to resolve velocities below 2 mm/yr.

We realized that with a large IGS global network added in our processing we can achieve more precise results than when we used only SOPAC solution because we combined daily solutions with homogeneous parameter estimation. We recognized that the global IGS network has a critically effect on the variability of the three coordinate components of regional sites. We observed a decrease of nrms and wrms which can reach a factor of 2 when combining with the global IGS network. Figure 15 shows the time-series of the THED site in NE of Iran, without and with combination with the global IGS network. Perhaps, the improvement of the coordinate variability refers to better adjustment of satellite orbits or more stable establishment of the reference frame ITRF. We therefore recommend that regional networks are combined with a global IGS network calculated with the same data analysis strategy, despite the additional time and equipment these calculations require. If this additional IGS solution is not feasible, it is possible to combine with SOPAC solution.

When we included ATML modelling for atmospheric loading and the VMF1 mapping function in the processing, the accuracy of the height component improved with respect to calculations without atmospheric loading and with a classical mapping function (Niell, 1996).

We observed in the time-series of the TOUS and NISH stations a periodic subsidence of around 20 and 6 cm per year, respectively (Figure 16). These stations are located in the NE of Iran close to Mashhad. The subsidences are probably related to strong variations of the ground water level. These high GPS inferred subsidences could be compared to levelling observations or INSAR data.

Computation is sensitive to the distribution of the sites of both the regional and global networks, for example in regions with a sparse distribution of stations we could not obtain results significant for kinematics and tectonics. A dense network with several stations on the same tectonic unit (e.g. a rigid micro block) provides redundant information which can be used to evaluate the measurement uncertainties by comparing the site velocities which should be coherent with rigid block motion. Differences could be due to site instabilities or a short data span which does not yet constrain a significant linear velocity.

Some of the permanent stations are located very close to faults such as the KSHM station in the Mashhad sub-network. When interpreting the displacement rate of such a station, the proximity to the fault and therefore the possibility that the site's motion is slowed down by deformation across the locked fault should be taken into account. A direct interpretation of the site velocity for geodynamic purposes is not possible.

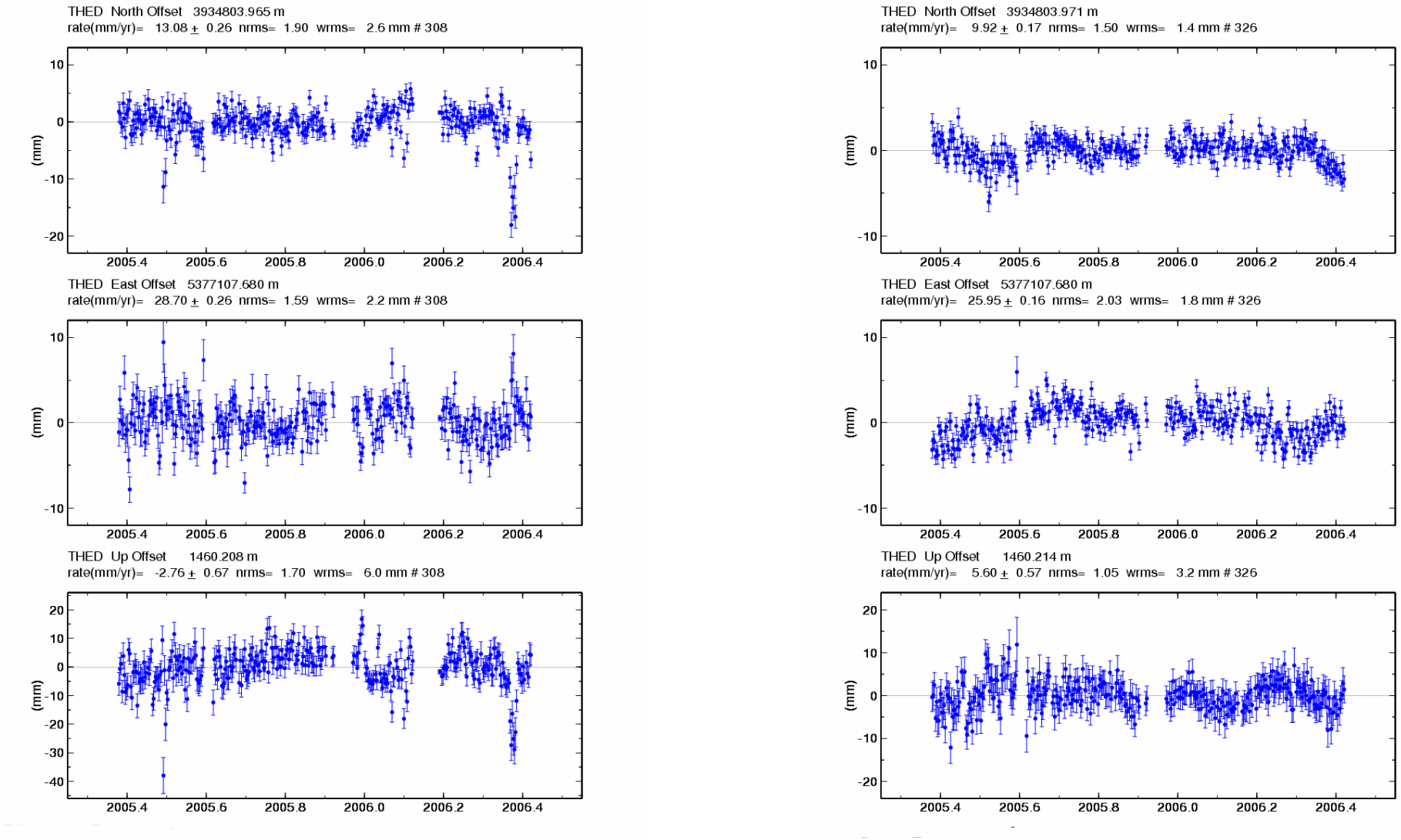

Figure 15: Time-series of THED site for the three components North-South (upper box), East-West (middle box), and Up-Down (dower box) at: Left panel: combination of the regional network without the global IGS network. Right Panel: combination of the regional network with the global IGS network. The horizontal axes show the time is in years and the vertical axes the site positions on each component whit respect to the weighted average position. The error bars indicates 1σ, and normalized (nrms) and weighted (wrms) root mean square scatters are plotted in mm.

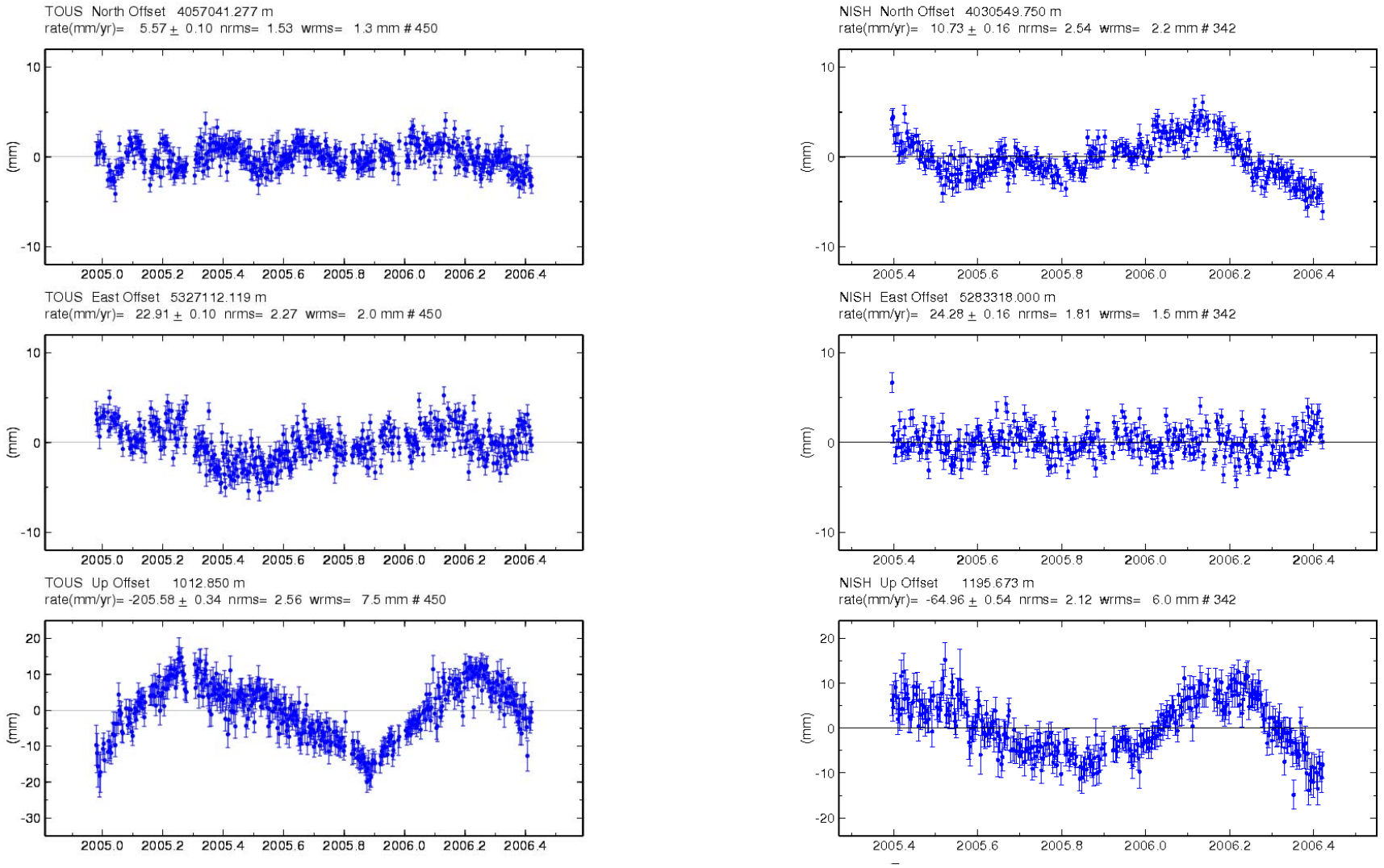

Figure 16: Figure 15. Time series of geocentric positions for the three components North-South (upper box), East-West (middle box), and Up-Down (lower box). Left panel: Tous (TOUS) site. Right Panel: Neishabour (NISH) site. The horizontal axes show the time in years and the vertical axes the site position on each component with respect to a weighed average position. The error bars indicate 1σ, and normalized (nrms) and weighted (wrms) root mean square scatters are plotted in mm.

We estimated the velocity field of Iran by combining Iranian permanent stations with some campaign measurements (e.g. on the Iran Global network or the North Zagros network). This velocity field is represented with respect to three different reference frames (see section 3.3.3). In particular, the velocity field of Iran with respect to the Eurasian rigid plate is shown on Figure 16. We marked the stations on the velocity field with different colour with respect to the monumentation date. The stations at the NE and E extremities of the Iranian territory show low velocities as they belong to the stable Eurasian plate. The IGS station BAHR (Bahrein) south of the Persian Gulf moves with the Arabian plate velocity at 22 mm/yr to the NNE with respect to Eurasia.

The site velocities shown in Figure 17 are presented with error ellipses representing a 95% confidence interval. Different stations have different formal errors. The age of the permanent stations and the interval covered by campaigns are the most important criteria for obtaining small uncertainties and therefore significant results. We estimated that a minimum of 2 years of permanent observations and 4 years of campaign type observations are necessary to resolve velocities below the limit of 2 mm/yr.

We combined permanent and campaign networks and could evaluated the coherence between the two types of measurement and the two types of station monumentation (Fig. 16). One example is the close by stations SFHN (permanent) and QOMS (campaign). Despite the SFHN station being young (observed less than 2 years), the inferred velocity corresponds closely to the QOMS station measured over 4 years. The difference is 6 mm/yr on N component and 0.9 mm/yr on E component, with uncetainity two times better on the campaign station (QOMS).

The compatibility between permanent and campaign sites are also tested by comparing the GRGN permanent site and the KORD Iran Global campaign site. The GRGN station is young with less than 2 years of observation, while the KORD station has been observed for the amplitudes of the two velocities are different, but the direction of movement is the same with degradation 1.5 times on the uncertainty of the KORD site. Indeed, these sites are situated in the NE part of Iran with a good regional coverage by permanent and campaign sites. This improves the consistency of the independent measurements.

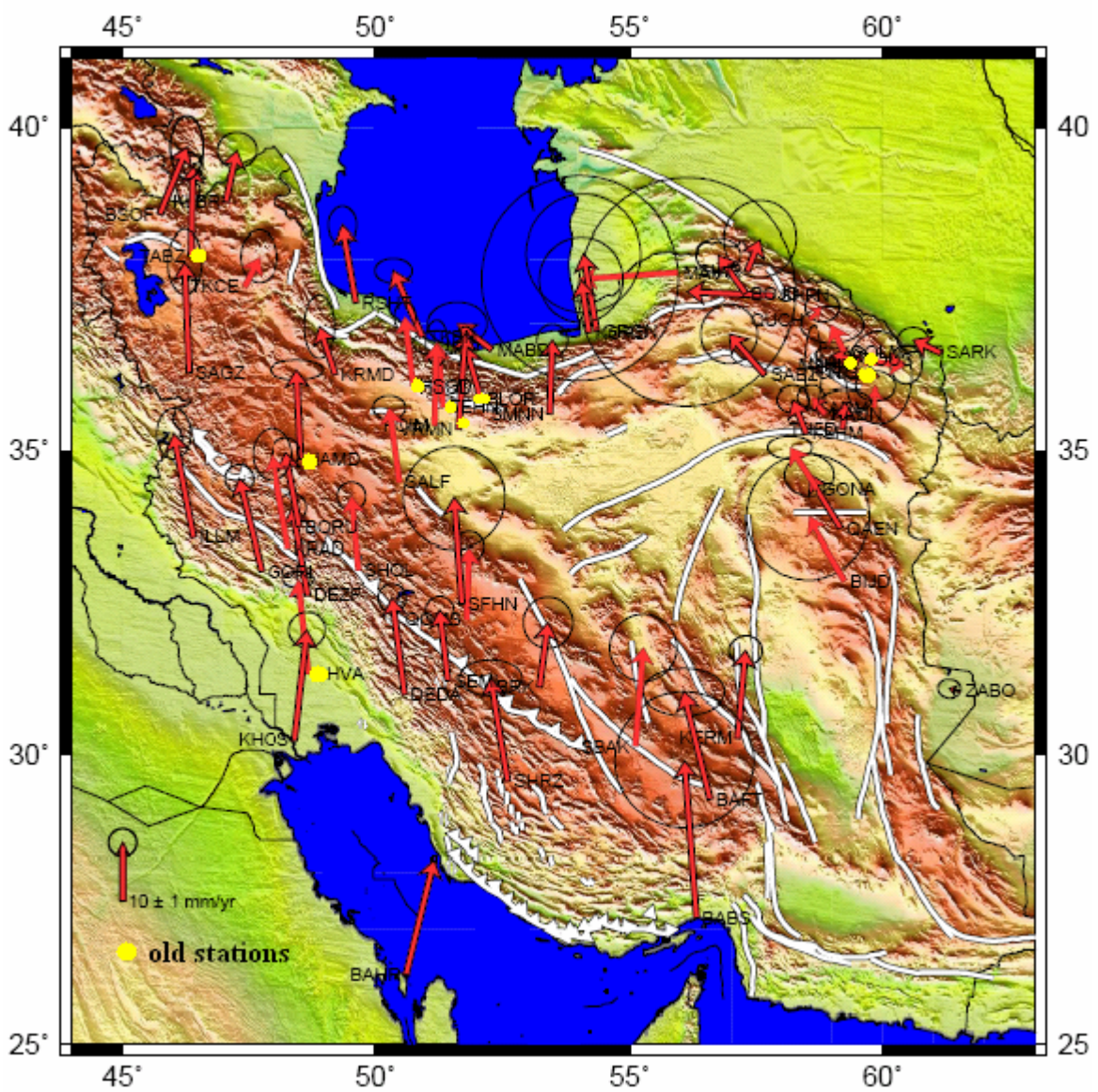

Figure 15 : Figure 16 The horizontal velocities with 95 percent ellipses in Eurasian-fixed reference frame from 2000 to 2006. The old stations that are monumented before May 2005 (see section 3.4) are marked by yellow circles.

In Figure 18 we compare two analysis strategies for the campaign networks: The solution prepared in this Master thesis uses the full time series of daily solutions on the Iranian permanent network and includes the campaign data at the epochs of campaign measurement (red vectors). The solution prepared in the PhD thesis of F. Tavakoli at LGIT uses the Iranian permanent station only during the measurement campaigns (blue vectors). The comparison shows that the continuity of the permanent network solutions from 2002 to 2006 caused significant improvements of the uncertainty of campaign stations. Significant improvements can be found for example on the Kerman (KERM) and QOMS stations.
Our processing of the IPGN data shows promising results for continuous monitoring of the present day kinematics in Iran, and for providing an efficient reference frame for campaign measurements in regional densification networks. At the end of this thesis, the combination of campaign networks and permanent data provide only first order results on the present-day kinematics, in particular because most of the permanent sites are still too young.

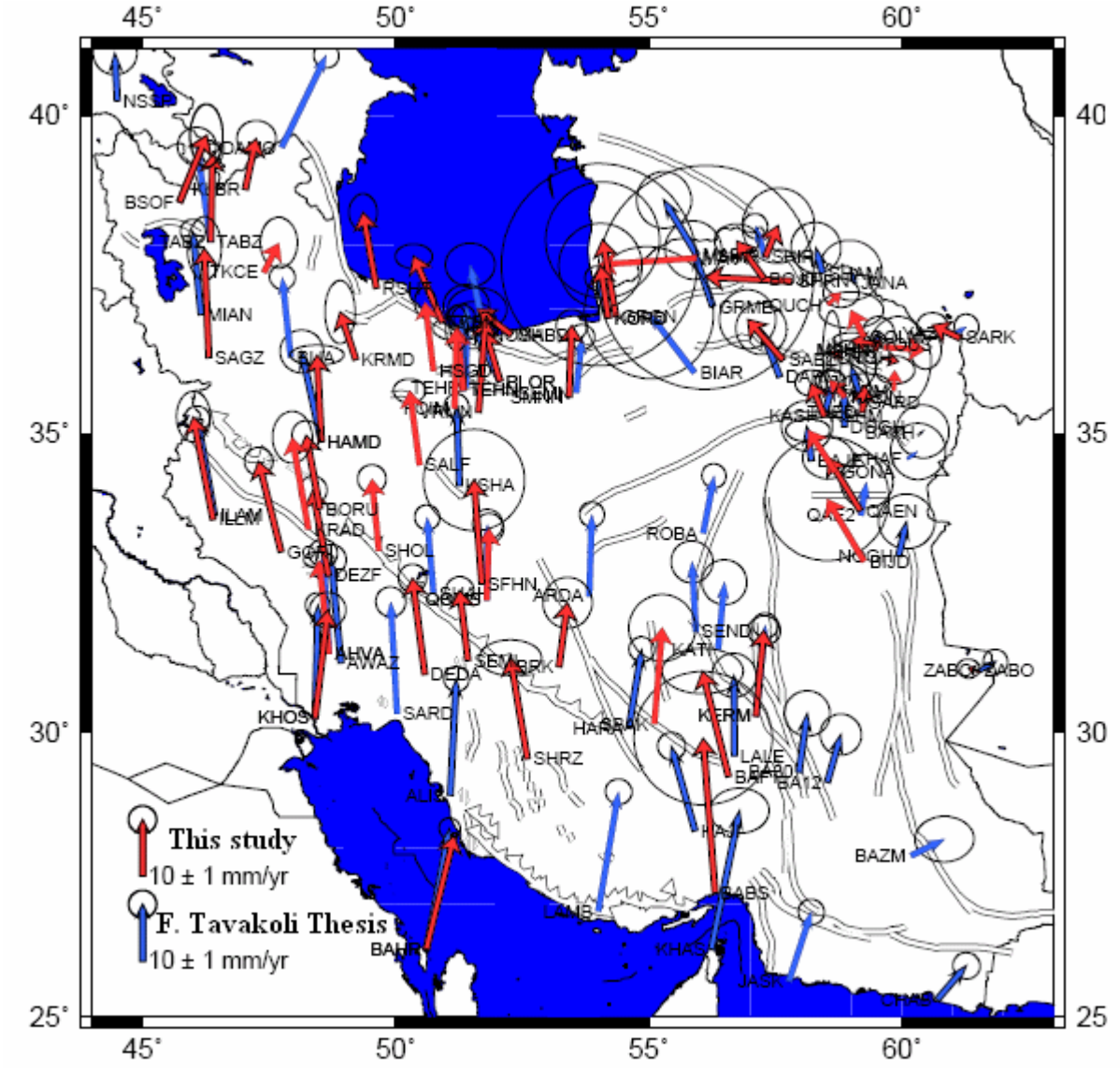

Figure 16 Comparison of the horizontal velocities of campaign and permanent stations, with 95 percent ellipses in Eurasian-fixed reference frame from 2000 to 2006. The result of this study is shown by red arrow and the result of only campaign stations processing (F. Tavakoli thesis) is shown by blue arrows.

According to Figure 16, the concentration of the GPS stations on the Lut block (our particular interest for the Modelling part) is still poor. This region was not a priority for the installation of permanent stations (no major city) and it is difficult to find safe places for campaign sites. The existing campaign and permanent stations are still too young at the time of this study to constrain significant tectonic displacements. However, in one year from now they will provide important new insights in the Lut block kinematics.

Part II

4 Modeling the Coulomb Stress Transfer between active faults bounding the Lut block

4.1 The studied earthquakes

4.1.1 The 1968 August 31 Dasht-e-Byaz earthquake (West)

The Dasht-e-Bayaz earthquake was occurred in Khorasan province (latitude 34°3.1'; longitude 58° 57'; Berberian and Tchalenco 1975; Ambraseys & Melville, C.P., 2005; Walker et al, 2004), on the 31st of August 1968. The moment magnitude is M_w 7.1 at the depth of the 17 km (Berberian and Tchalenco 1975; Ambaraseys & Melville, C.P., 2005; Walker et al, 2004). The determined source parameter and moment magnitude is summarized on the table 4.

This earthquake produced 80 km of surface ruptures on the Left lateral strike-slip Dasht-e-Bayaz fault, from longitude of 58°35E to east of Zigan, at longitude of 59°25E (Figure 19), obviously caused extensive damage in the region, mostly in the Nimbluk valley where many houses and populated were completely destroyed (Ambaraseys & Melville, 2005).

Ambraseys and Tchalenko (1969) and Berberian and Tchalenco (1975) reported that the horizontal surface displacement ranges from 0 to 4.5 meters and that the vertical displacement ranges from 0 to 2.5 meters. The average displacement is about 2 meters.

Acoording Niazi (1969) study shows that the source of this event has been had multiple sources for the main shock and the rupture propagated that at times decelerated with the pause of the several seconds, the free inversion of long period waveform studies indicate that 90 percent of the moment was released in the roughly east west left-lateral strike-slip faulting that produce the surface ruptures, though probably in several sub-events. And 10 percent of moment may have been related with a sub-event involving thrust.

In total between 7000 to 12000 people were killed and at least 70000 made homeless, The trace of earthquake fault was extended from the west of Dasht-e-Bayaz fault (Kuhe Siah range) across Nimbluk vally to the Kuhe Meykey Mountain in the east.

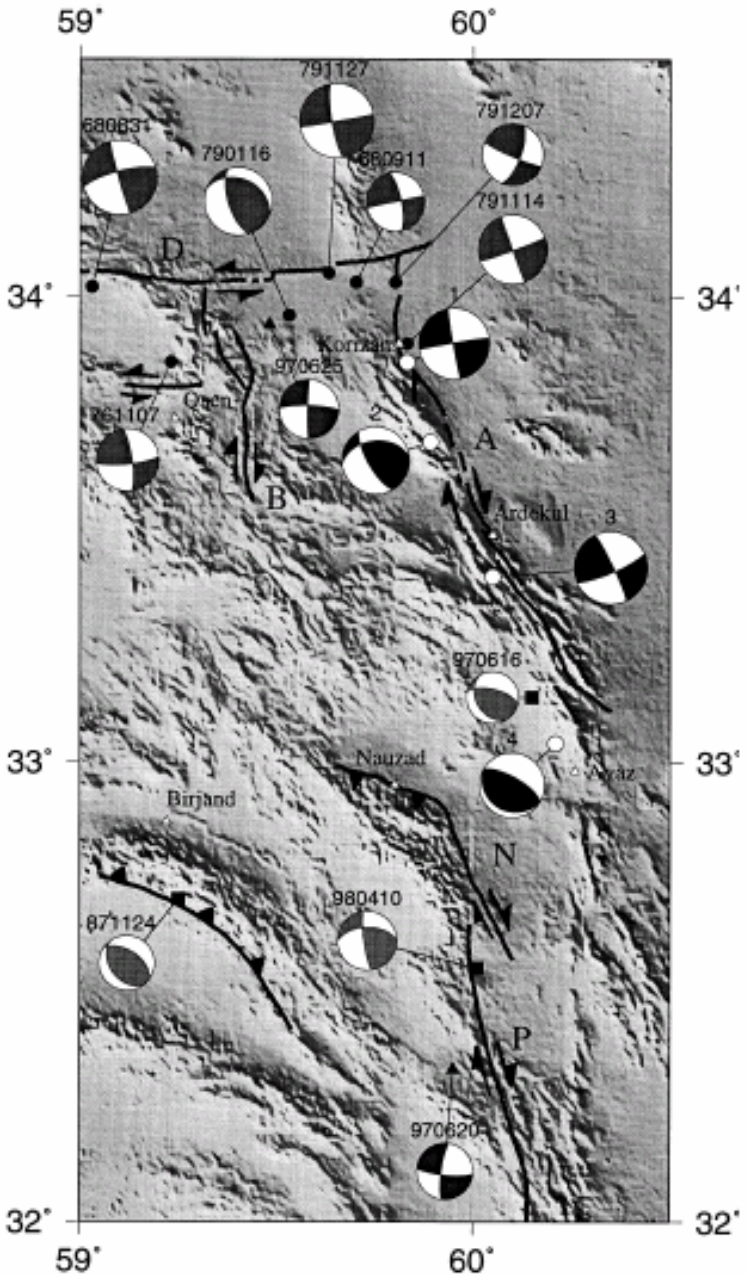

Figure 19: Summary map of the faulting, topography and focal mechanisms in the northern Sistan suture zone. White circles and their accompanying focal spheres marked 1-4 are the locations and mechanisms of the four sub-events used to model the main-shock of the 1997 May 10 earthquake. Black triangles are the locations of the largest aftershocks of 1997 June 16, 20 and 25, Other events, with their CMT mechanisms from Harvard, are located by black squares. Identified fault systems are: A-Abiz; B-Boznabad; D-Dasht-e-Bayaz; N-Nauzad; P-Purang. (Berberian et al 1999)

4.1.2 The 1979 November 27 Khuli-Buniabad earthquake

A number of shallow earthquake occurred in the Qaenat area in the NE of Iran, starting on November 14 1979 to December. The most destructive earthquake occurred on 27 November that its epicenter was located at latitude 34.06N and longitude 59.76E, with moment magnitude 7.1 (Mw=7.1 Ms=7.1), with focal depth in 8 km (Walker et al,2004), surface rupture developed along capable faults through the bedrock and Quaternary deposits. And it accompanied a 60-km E-W trending left-lateral fault rupture on Dasht-e-Bayaz left lateral strike-slip on the east. Also, the northern end of the earlier rupture continued

northeastward to align with the eastern end of the second rupture on the right lateral strike-slip Abiz fault around 10 km. (Haghipour et al 1980); but Berbeian et al (1999) identify the aftershock on 7th December 1979 Kalat-e-Shur earthquake was responsible of this rupture. In fact it was affected between villages of Chah-e-Zandar and Buniabad.(Ambaraseys and Melvile, 2005).

Evidently this earthquake was re-ruptured 10km of surface faulting in 1968 Dasht-e-Byaz earthquake which is continued east of Zigan. There is no precisely observation on the displacement in lateral and vertical component, according to the several papers as Haghipure and Amidi 1980 and Ambraseys & Melville (2005) reported that maximum lateral offset 1-4 meter and vertical displacement is up to 2.5 meter.

Because this region is slightly populated, so it caused a few number inhabitant and death. (Ambaraseys and Melvile, 2005; Haghipure and Amidi 1980; Walker et al, 2004).

4.1.3 The 1997 May 10 Zirkuh earthquake (Abiz fault)

The destructive Zirkuh-e-Qa'enat earthquake of 1997 May 10 with moment magnitude of 7.2 (Mw 7.2, Ms 7.3, mb 6.3) occurred at the atitude 33.81N and longitude 59.81E, in the Zirkuh district of eastern Iran. It occurred in the Sistan suture zone which is the located along the eastern border of Iran, at the boundary with Afghanistan. The Sistan suture zone consists of predominantly NNW-SSE right-lateral strike-slip faults along the Abiz fault system, and of a series of N-S faults (Berberian, 1983; Jackson & McKenzie, 1984).

The earthquake nucleated in the northern part of the Abiz fault system and ruptured 125 km of NNW-SSE right- lateral strike-slip surface. It broke parts of the Abiz fault that ruptured the surface in previous earthquakes in 1936 and 1979. At the northern end of the 1997 ruptures the N-S right-lateral strike-slip system changes to another system of E-W left-lateral strike-slip faults (Figure 19), some of which have also moved in large earthquakes within the last 30 years (Ambraseys & Tchalenko, 1969; Haghipour & Amadi, 1980; Berberian & Yeats, 1998).

Thus, in addition to its inherent interest as a major earthquake involving surface rupture in four sub-events (Berberian et al., 1999), the Zirkuh earthquake has a wider significance for how strike-slip faults re-ruptured in earthquakes, for how the motion between Arabia and Eurasia is absorbed in Iran, and for the behavior of conjugate domains of strike-slip faults in regions of distributed continental tectonics.

The amplitude of the lateral displacement and vertical displacement varied along the trace of the Abiz fault within 0.8 meter to 1.4 meters, with maximum lateral slip of 2.3 meters and and maximum dip slip of 0.90 meter. Berberian et al. (1998) have significant observations along this trace. We mainly used this observation in the modeling (Table 6 and 7).

Particularly to the previous earthquake in 1979 eastern of Dasht-e-Bayaz , because of the low population density in that region and regarding to working time (12:28 pm local time) many people were outside and because of warning foreshock approximately 10 second before main shock, however the main shock killed around 1568 and injured 2600, but completely destroyed 12 000 houses and damaged more than 7000 houses in 147 villages in the Qa'en, Birjand and Khaf counties of the Khorasan province in eastern Iran(Berberian et al 1999).

4.2 Coulomb stress failure and Coulomb stress change theory

4.2.1 Coulomb stress failure

The tendency of rocks to fail in a brittle manner is thought to be a function of both shear and confining (normal) stresses, commonly formulated as the Coulomb failure criterion.
The brittle rock failure occurs on a plane when the Coulomb stress σ_f exceeds a specific threshold value:

$$\sigma_f = \tau_\beta - \mu(\sigma_\beta - \rho) \quad (1)$$

Where
τ_β is the shear stress on the failure plane
σ_β is the normal stress
ρ is the pore fluid pressure
μ is the coefficient of friction

Notice that the value of τ_β must always be positive in this expression, whereas the usual processes of resolving stress onto a plane may give positive or negative values depending on whether the potential for slip on the plane is right- or left-lateral. The sign of τ_β must therefore be chosen appropriately, i.e. in the sense of slip. (King et al, 1994)
If the failure plane is orientated at β to the $\sigma 1$ axis we can express the stress components applied to it in terms of the principal stresses:

$$\sigma_\beta = \frac{1}{2}(\sigma_1 + \sigma_3) - \frac{1}{2}(\sigma_1 - \sigma_3)\cos 2\beta \quad (2)$$

$$\tau_\beta = \frac{1}{2}(\sigma_1 - \sigma_3)\sin 2\beta \quad (3)$$

Where $\sigma 1$ is the greatest principal stress and $\sigma 3$ is the least principal stress. Equation (1) then becomes

$$\sigma_f = \frac{1}{2}(\sigma 1 - \sigma 3)(\sin 2\beta - \mu\cos 2\beta) - \frac{1}{2}\mu(\sigma_1 + \sigma_3) + \mu\rho \quad (4)$$

Differentiating equation (4) as a function of β, one finds that the maximum Coulomb stress σ_f^{max} occurs when

$$\tan 2\beta = \frac{1}{\mu} \quad (5)$$

Pore fluid pressure modifies the effective normal stress across the failure plane as shown in equation (1). When rock stress is changed more rapidly than fluid pressure can change through flow, ρ can be related to confining stress in the rock by the Skemptons coefficient β, where β varies between 0 and 1. Equation (4) and subsequent expressions can therefore be rewritten on the assumption that $\sigma\beta$ represents the confining stress as well as the normal stress on the plane (Simpson and Reasenberg 1994):

$$\sigma_f = \tau_\beta - \mu'\sigma_\beta \quad (6)$$

where the effective coefficient of friction is defined by $\mu' = \mu(1-\beta)$.

4.2.2 Coulomb stress changes on faults of specified orientation

Regarding to the Figure 20, imagine that in a system where the x- and y-axes and fault displacements are horizontal plane, and fault planes are vertical (z direction), stress on a plane at an angle ψ from the x-axis can be expressed by:

$$\sigma_{11} = \sigma_{xx}\cos^2\psi + 2\sigma_{xx}\sin\psi\cos\psi + \sigma_{yy}\sin^2\psi$$
$$\sigma_{33} = \sigma_{xx}\sin^2\psi - 2\sigma_{xx}\sin\psi\cos\psi + \sigma_{yy}\cos^2\psi \quad (7)$$
$$\tau_{13} = \frac{1}{2}(\sigma_{yy} - \sigma_{xx})\sin 2\psi + \tau_{xy}\cos 2\psi$$

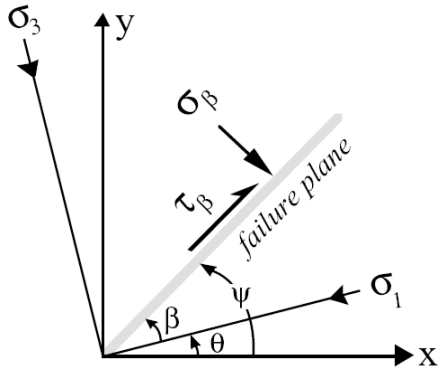

Figure 20: coordinate system used for Coulomb stress calculation from King et al 1994

So the Coulomb stress changes for right-lateral σ^R_f and left-lateral σ^L_f motion on plane oriented at the ψ with respect to the x axis will be written as:

$$\sigma_f^R = \tau_{13}^R + \mu'\sigma_{33} \quad (8)$$
$$\sigma_f^L = \tau_{13}^L + \mu'\sigma_{33} \quad (9)$$

Notice that the sign of the τ_{13} from equation (7) is unchanged for right-lateral slip (τ^R_{13}) in equation (8) and reverses in sign for left-lateral slip (τ^L_{13}) in equation (9).

Figure 21.a (King et al., 1994) illustrates equations 8 and 9. An elliptical slip distribution is imposed on a right lateral strike-slip master or primary fault in a uniform, stress-free, elastic half-space. The authors calculated the Coulomb stress change due to this source on secondary planes (or receiver planes) which correspond to right lateral strike-slip faults parallel to the master fault. The left and middle panels of the figure 21.a show the calculated shear and normal stresses, respectively, on the secondary planes. The shear stress equals the traction resolved on an assumed slip vector within the secondary fault plane, and the normal stress equals the traction resolved on the normal vector to the secondary fault plane. The right panel represents the change of Coulomb stress on these planes resulting only from slip on the master fault. To realize this calculation, one need only to know (1) the seismic source parameters and geometry of the master fault, (2) the geometry and mechanism of faulting of the secondary plane and (3) the coefficient of friction. This calculation is independent of any knowledge of existing regional stress or any pre-existing stress field from other events. The signs in the calculation are chosen such that a positive Coulomb stress change indicates a tendency for slip in the defined sense of slip on the receiver fault (right lateral slip in the example).. Negative Coulomb stress change indicates a reduction of this tendency. In this example, as in all strike-slip cases, the positive stress change lobes appear at the fault ends, subsequent to the stress concentration that have a tendency to propagate along the faults. Small off-fault positive lobes also appear, separated from the fault by a region

where the Coulomb stresses have not been increased. These off-fault positive lobes result from the Coulomb normal stress change that increases the tendency of off-fault to fail. The Coulomb normal stress also reduces the symmetry of the final distribution of stresses.

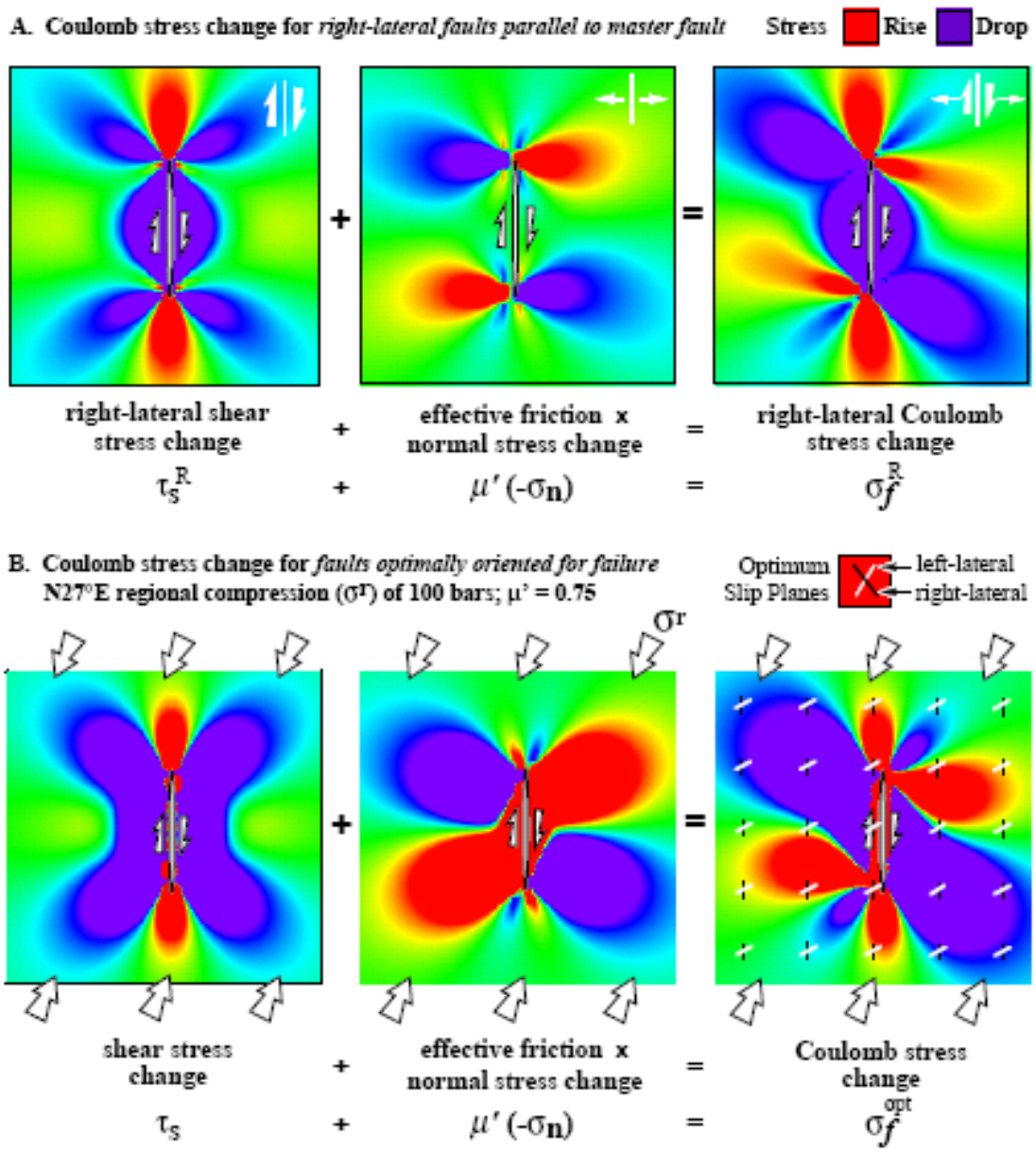

Figure 21: Coulomb stress change examples. The top panels show the calculation of the shear (left), normal (middle) and total (right) Coulomb stress change due to an earthquake that occurred on a N-S vertical right lateral strike-slip master fault on N-S right lateral strike-slip receiver faults. The master fault is embedded in an elastic half-space, and the calculation is independent of any regional stress field. The bottom panels show the calculation of the shear (left), normal (middle) and total (right) Coulomb stress change due to the same source on optimally-oriented strike-slip faults. The calculation of the optimally-oriented faults depends on the regional stress field represented by the white arrows. The colored background represents the Coulomb stress change.

4.2.3 Coulomb stress failure on optimally-oriented faults

Coulomb stress change on the optimally-oriented plane can also be calculated as a result of slip on master fault plane (source fault) and these the planes on which aftershocks might be expected to occur. For the calculation, we need to consider all range of plane orientations and mechanism of slip for the receiver plane in the surrounding of the master fault. Moreover, we also need to know the regional stress orientation because the optimally-oriented fault for failure is a function of the existing regional stress and the stress associated with the master fault (and the fault friction coefficient) (King et al., 1994).

Figure 21.b show the calculation of the optimally-oriented strike-slip plane for the same seismological source parameters and geometry parameters for the master fault as in figure 21.a. The optimum orientations (left and right lateral strike-slip) are calculated from the total stress after the earthquake, and the Coulomb stress changes caused by the earthquake stress changes are resolved onto these planes. On the optimally-oriented plane where the failure is promoted, small earthquakes (aftershocks) are expected to occur.

4.3 Modeling the Coulomb stress changes

4.3.1 The Coulomb 3.0 software

- The software

We use the Coulomb 3.0 software, written by S. Toda, R. Stein, J. Lin, V. Sevilgen (2007) (http://www.coulombstress.org) to calculate the variation of the static Coulomb stress caused by fault slip at any surface and any depth in an elastic half-space with uniform isotropic elastic properties.. The program implements elastic dislocation formulae of Okada (1992).

- The input data

To run a calculation, one needs to define different kind of parameters, in particular the parameters that describe the source and the receiver fault. The source is described with the rupture parameters of the source (slip, depth, length, and rake) and the geometry of the broken fault (strike and dip angles). The receiver fault plane on which we calculate the Coulomb stress plane is described with its geometry and mechanism of faulting (strike, dip, and rake). Conventions of Aki and Richard (1980) are used for these parameters.

Moreover, we need to fix the coefficient of friction of the receiver fault as well as the elastic parameters of the elastic half-space. The coefficient of friction is commonly found to be 0.6 to 0.8 for laboratory samples (Lachenbruch and McGarr, 1990), but in stress triggering studies it is inferred to range anywhere from 0 to 0.8. Stein [1999] noted that smaller/larger values of the effective coefficient appear to be correlated with the maturity/immaturity of the secondary fault zone. The calculations are very sensitive to the friction coefficient. The fault we model (Dash-e-Bayaz and Abiz faults) are young system. The age of this system is probably less than 200 million years old (Jackson et al 2004). In most of the following calculations, we fix the effective coefficient of friction to 0.4 as we do not have much information on the maturity of the faults we study. We also assign an average value of 0.25 to the Poisson ratio, and of 8x105 bar to the Young‘s modulus. The value for the shear modulus is then $3.3x10^{10}$ Pascal.

4.3.2 Rupture parameters

We use information taken from the literature to describe the source parameters and the geometry of the primary earthquakes. The information that we found come from different sources:

- Berberian and Tchalenco (1975) study on the 1968 earthquake and Berberian et al. (1999) study on the 1997 Zirkuh earthquake (called Berberian in the following tables).
- Walker et al. (2004) study on the 3 major earthquakes (called Walker in the following tables).
- USGS catalogue provided by US geological survey
- Manighetti 's cartography (pers. comm., 2007) corresponding to a detailed surface rupture map focused on the studied area and derived from satellite images (Landsat) and precise MNT (called Manighetti in the following tables).
- Manighetti's earthquake catalogue (pers. comm., 2007) corresponding to a synthesis of the Engdhal and Ambaraseys and Melvile, 2005 earthquake catalogues with its rupture map (called Manighetti in the following tables).

Given the different information found, we optimized the source parameters according to the data collected by Berberian and Tchalenco (1975), Berberian et al. (1999) and Walker et al. (2004) for each earthquake, and the detailed surface rupture obtained by Manighetti (pers. comm., 2007) (i.e. the length obtained from the Manighetti detailed fault map). We use the calculation of the seismic moment (and the moment magnitude Mw) to check the parameterization of the source checking that the modelled seismic moment is consistent with all the observed seismic moments found in the literature. The scalar seismic moment M0 is defined by the following equation

$$M_O = \mu A u \qquad (10)$$

Where - μ is the shear modulus, in this study we fix it to 3.3×10^{10} Pascal; - A is the area of the rupture with $A = LW$ (L =length of rupture and W=width of rupture; -u is the average displacement on A (net slip).

The moment magnitude M_w is a scale introduced in 1979 by T.Hanks and H. Kanomori as a successor to the Richter scale. M_w is used by seismologists to compare the energy released by earthquakes. The moment magnitude M_w is dimensionless number defined by:

$$M_w = \frac{2}{3}\left(\log_{10}\frac{M_0}{N.m} - 9.1\right) = \frac{2}{3}\left(\log_{10}\frac{M_0}{dyn.cm} - 16.1\right) \qquad (11)$$

Where M_0 is the seismic moment.

- **The 1968 Aug 31 earthquake (S1)**

According to the Table 4, related to the 1968 August 31, we model the rupture of this event along the East Dasht-e-Bayaz fault as one left lateral strike-slip segment of 80 km length and 15 km depth. We examine all fault geometries which are listed on the table to get the average orientation of the fault as close as possible as the mapped rupture. We decide to fix the strike to 254°N, the dip angle to 84° and the rake to 5°. With all these parameters, we calculate the moment magnitude to find the good average slip on this fault plane and check that the slip and moment magnitude are correct with the values given in the literature. We then use an average slip of 1.68m, uniform on the fault plane, a seismic moment of 6.65×10^{19} N m and a

moment magnitude of 7.14 consistent with the value summarized in table 4. As we use only one segment and a uniform slip to model this large event, we tapered the slip on the fault plane. In this way, the amount of slip on the edge of the plane is lower than the amount of slip on the centre of the plane.

1968 Aug 31 lat: 34.02N Long 59.03 Dasht-e-Byaz(West)

	USGS	Berberian et al	Maneghetti et al	Walker	my study
Strike (deg)	-------	-------	75	254	254
Dip(deg)	-------	-------	-------	84	84
Rake(deg)	-------	-------	-------	5	5
Depth(km)	-------	15	15	17	15
M_o(Nm)	-------	-------	-------	-------	$6.65x10^{19}$
Mw	7.1	7.2	7.3	7.1	7.1
Length (km)	70	80	80	80	80
Lateral slip(m)	-------	4	6	4.5	1.62
Vertical slip(m)	-------	1	2.5	2.5	0.475
max net slip(m)	5.4	4.1	6.5	5.1	-------
Ave Net slip(m)	-------	-------	-------	-------	1.68

Table 4: source parameters of the 1968 Aug 31 earthquake

- **The 1979 Nov 27 earthquake (S2)**

For the East Dasht-e-Bayaz earthquake, we assume two segments with respect to the rupture that extends on two different fault types. The earthquake broke 60 km of the ~E-W left lateral strike-slip Dasht-e-Bayaz fault and approximately 8 km of the ~N-S right lateral strike-slip Abiz fault. We make the hypothesis that these two segments slipped identically because there was no instrumental measurement evidence for this parameter. We then assign the same slip value for both segments. The fault geometry and earthquake properties are summarized in table 5. We also tapered the slip on the 60km segment.

1979 Nov 27 at Lat:34.05°N & long:59.63°E Dasht-e-Byaz(East)

	USGS	Manighetti et al	Walker	my study
Strike (deg)	267	80	261	261
Dip(deg)	-------	-------	82	82
Rake(deg)	-------	-------	8	8
Depth(km)	25	8	8	15
M_o (Nm)	$4.6x10^{19}$	-------	-------	$4.16x10^{19}$
M_w	7.1	7.1	7.1	7.1
Length (km)	-------	68	60	68
Lateral slip (m)	-------	4	4	1.37
Vertical slip (m)	-------	3.90	2.5	0.0
max net slip (m)	-------	3.90	-------	-------
Net slip (m)	-------	-------	-------	1.37

Table 5: source parameters of the 1979 Nov 27 earthquake

- **The 1997 May 10 earthquake (S3) and its aftershocks**

The 1997 May 10 earthquake occurred on the Abiz fault trace. This earthquake was possibly a complex earthquake involving 4 sub-events (Berberian et al., 1999) that generate a complex rupture (more than 4 segments). We examine both average source parameters and individual source parameters of each sub-event that are characterized by Berberian et al (1999). The detailed of these parameters is summarized in the Table 6 and 7 respectively.

1997 May 10 at Lat:33.86N & Long:59.83 Abiz fault

	USGS	Manigetti et al	Berberian	my study
Strike (deg)	-------	-------	156	156
Dip(deg)	-------	-------	89	89
Rake(deg)	-------	-------	-160	160
Depth(km)	10	15	13	15
Mo(Nm)	-------	-------	-------	7.66×10^{19}
M_w	7.2	7.2	7.12	7.2
Length (km)	125		125	125
Lateral slip(m)	2.3	2.3	2.3	2.3
Vertical slip(m)	0.9	0.9	0.9	0.9
max net slip(m)	-------	3	3	-------
Net slip(m)	-------	-------	-------	2.46
Dip slip(m)	-------	0.9	0.9	0.9

Table 6: source parameters of the 1997 May 10 earthquake

	Strike (deg)	Dip (deg)	Rake (deg)	Length (km)	Depth (km)	net slip(m)	Lateral slip(m)	Dip slip(m)	M_o (Nm)	M_w
Event 1	170	88	178	12 / 15	9	1.52	1.48	0.35	2.03×10^{19}	6.8
Event 2	150	71	127	30	10	0.91	0.67	0.625	1.35×10^{19}	6.6
Event 3	335	90	180	61	10	1.30	1.30	0.00	3.92×10^{19}	7.0
Event 4	120	20	90	7	10	1.04	0.60	0.85	0.36×10^{19}	6.3
							Total Seismic Moment		7.66×10^{19}	7.2

Table 7: fault mechanism of each sub-event on 10th of May 1997 according to Berberian et al 1999 characterization

Aftershocks of the 1997 Zirkuh earthquake were distributed on the surrounding of the Abiz fault system and of the Dasht-e-Bayaz fault system. The three aftershocks of magnitude higher than 5 are listed in Table 8. The first one that occurred on June 16 has the same fault mechanism thanthe fourth sub-event (Harvard CMT, Berberian et al., 1999).

The second aftershock that occurred on June 20 is located about 100 km south of the southern end of the 1997 Zirkuh ruptures. According to the P- and S-waveform inversion solution, it has the N-S right lateral strike-slip mechanism that characterizes the faulting mechanism in the region (Berberian et al., 1999). This earthquake maybe happened on the Purang fault but there where no information which is indicated the surface faulting in this region. Finally, the third aftershock that occurred on June 25 is located 20-40 km west of the northern end of the 1997 Zirkuh ruptures.

It also has a N-S right lateral strike-slip mechanism (derived from P- and SH-waveform inversion solution). Berberian et al. (1999) suggest that this aftershock, as well as

the 1979 Jan 16 earthquake occurred on one of the N-S right-lateral faults, such as the Boznabad and Parak faults, rather than on the E-W Dasht-e-Bayaz fault.

	Strike(deg)	Dip(deg)	Rake(deg)	Depth(km)	M_o(Nm)	M_w
16 June 1997 at 03:00:04 UST; 33.147N, 60.155E; Mb 5.0						
	120	20	90	10	------	5.0
20 June 1997 at 12:57:32:3 UST; 32:330N, 59:960E; Ms 5:4, mb 5:0						
	188	79	180	2	$1.4*10^{17}$	5.4
25 June 1997 at 19:38:40:6 UST; 33:94oN, 59:48oE; Ms 5:8, mb 5:6						
	181	87	170	8	$4.9*10^{17}$	5.7

Table 8: Source parameters of the principal Zirkuh aftershocks (Berberian et al 1999)

4.3.3 Strategy of Modeling

In the following, we call the 1968 Aug 31 source 1, S1; the 1979 Nov 27 source, S2; and the 1997 May 10 source, S3. In the same way, we call the 1979 Nov 27 receiver fault plane, R2; and the 1997 May 10 receiver fault plane, R3 when we assume an average fault plane for the whole rupture, and R3E1to R3E4 when we use the focal mechanism of each sub-event of the 1997 Zirkuh earthquake as receiver fault plane.
We first calculate the Coulomb stress change due to S1 on the 1979 E-Dasht-e-Bayaz fault rupture (R2). Then we calculate the Coulomb stress change due to S1 plus S2 on the average Abiz fault rupture (R3). We expend our investigation calculating the Coulomb stress change on R3E1-4. With these first models, we investigate if there is a Coulomb stress transfer relationship between the three large earthquakes.

Secondly, we investigate the stress perturbation due to S1 plus S2 and due to S1 plus S2 plus S3 on the surrounding area. In particular, we calculate the Coulomb stress change due to S1, S2 and S3 on optimally-oriented fault plane to examine the relation between the large earthquake and the seismicity. Specifically for the 1997 May 10 earthquake, we study if the three first aftershocks are consistent with Coulomb stress change pattern due to S3. Finally, with the optimally-oriented tests we examine which faults have its potential to fail increased to determine the zones or faults that need to be survey carefully in the future.

For all subsequent calculations in which we calculate the stress change on optimally-oriented fault plane, we specify the pre-existing regional stress orientation (see section 4.2.3). We extract the regional stress orientation in the Lut block from the World Stress Map (http://www-wsm.physik.uni-karlsruhe.de) database (Heidbach et al 2007). This map, zoomed on the Iranian region, is presented in Figure 22. Masson et al. (2005) derived the strain rate field in Iran from seismological and GPS data. Both stress and strain rate fields are consistent together. The direction of maximum shortening is closed to the direction of maximum compressive thrust in the Lut block area. We thus assume that the most compressive axis in this region is oriented N45°E with a 0° dip.

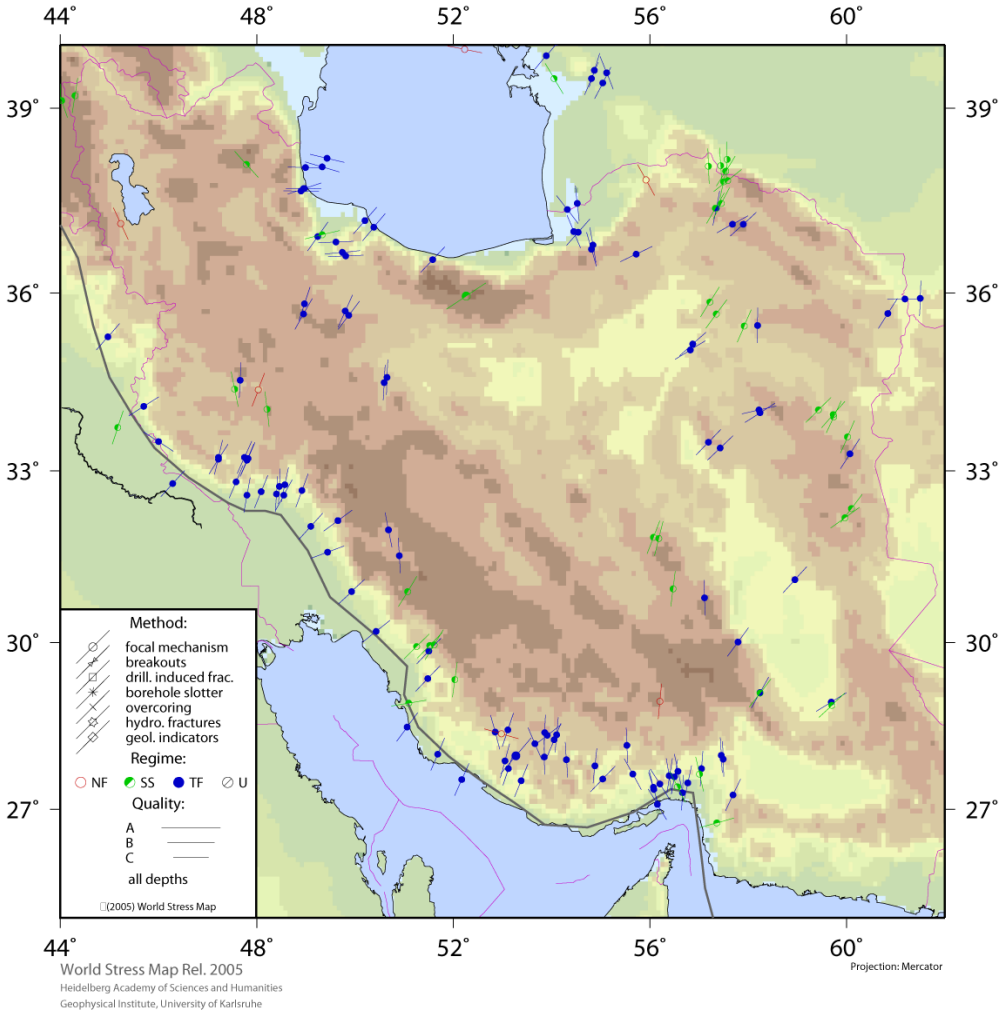

Figure 22: Stress direction and stress regime in Iran from World Stress Map agency

4.4 Results and discussion

4.4.1 The influence of the 1968 earthquake (S1) on the 1979 earthquake

We modelled the Coulomb stress changes caused by S1 (Table 4) on the east left-lateral Dasht-e-Bayaz fault (261°N) and the northern part of the N-S right lateral Abiz fault (170°N) where the 1979 earthquake sequence occurred. The result is presented on Figure 23. It shows that the stress increase by 1 to 5 bar on the rupture plane of the 1979 main shock earthquake. We then suggest that the 1968 earthquake triggered the 1979 main shock. The catalogue of USGS is incomplete before 1974 04 29, so we could not examine the influence of the 1968 earthquake on the successive seismicity.

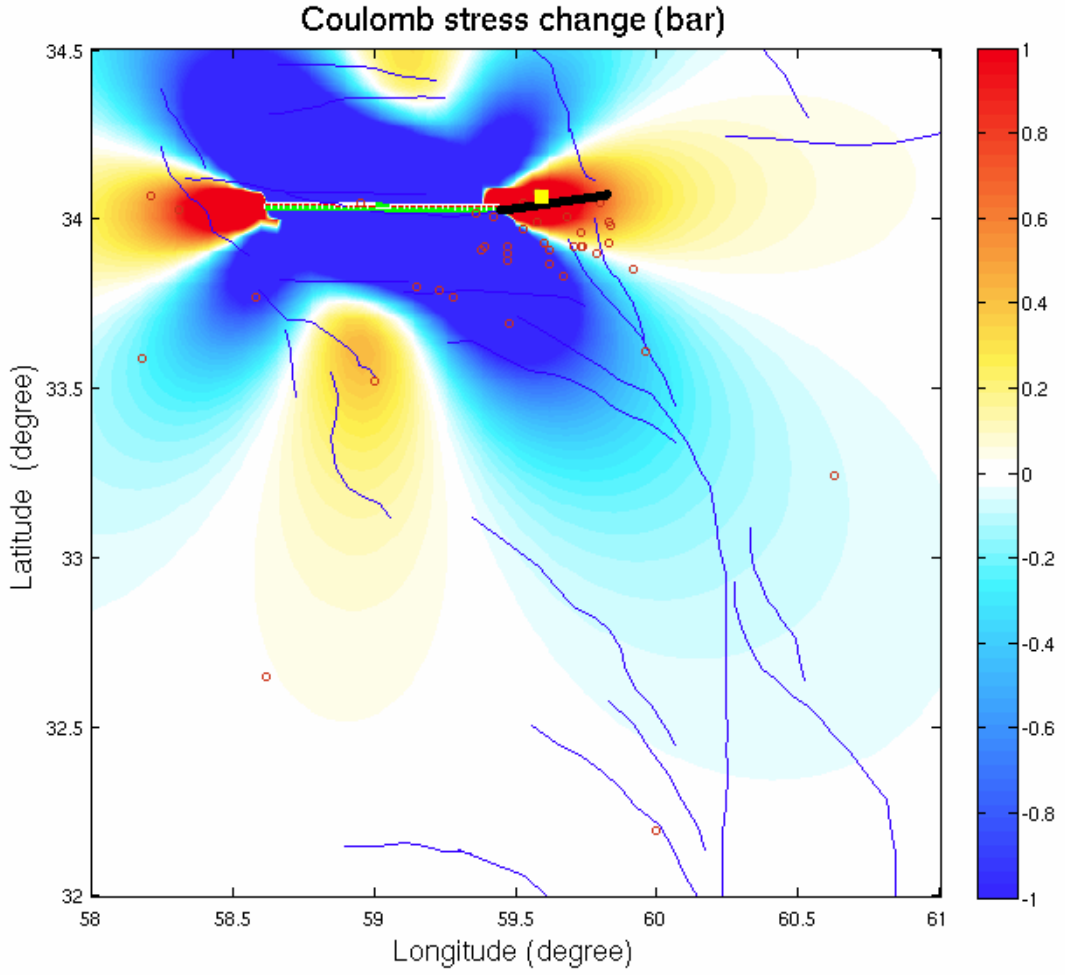

Figure 23: Coulomb stress changes from the 1968 Aug 31 earthquake (see Table 4) at depth of 8 km on 261°N left-lateral strike slip fault , corresponding to the east part of the Dasht-e-Bayaz fault that broke on the 1979 Nov 27. The background colour scale is in bar. The 1979 main rupture is represented by a thick black line, the 1979 main shock is represented with a yellow rectangle, seismicty is accompanying from 1974 04 29 to 1979 Nov 27 (USGS) by red circle.

4.4.2 The influence of the 1968 and the 1979 earthquakes on the 1997 May 10 earthquakes

Berberian et al (1999) show that the 1997 May 10 Zirkuh earthquake produced a complex, segmented series of predominantly right-lateral strike-slip surface rupture. It counted at least 4 different co-seismic segments that lie roughly along the Abiz fault system. Due to complexity of rupture plane, we performed several testes to see the influence of the 1968 (S1) and 1979 (S2) earthquakes on 1997 May 10.

First, we calculate the Coulomb stress changes caused by S1 and S2 sources on a receiver plane that satisfy the whole 1997 rupture plane. The average rupture plane corresponds to a 156°N right lateral strike-slip fault (Table 6). Figure 24 presents the result and shows that the most of the Abiz rupture lies in region where stress is reduced (up to -12 bars). Then the potential of the whole Abiz fault to fail decreased under the influence of the 1968 and 1979 main-shocks. Nevertheless, the northern part of the Abiz fault, where the rupture start according to Berberian et al 1999, is loaded by the 1968 and 1979 earthquakes.

The variation of Coulomb stress reach up to 0.4 bars in this area. As positive variation of Coulomb stress of 0.1 to 1 bar is sufficient to triggered an earthquake (Stein, 1999), this result show that the 1968 and 1979 encourage the rupture of the northern part of the Abiz fault.

Berberian et al. (1999) found that the observed waveforms of the 1997 Zirkuh earthquake are best fitted when they assumed the existence of 4 sub-events occurring sequentially form north to south (Figure 19). The Table 7 summarized the parameters of these four sub-events. We are interested in the first sub-event (170°N, 88° dip, righ-lateral strike-slip) which is located in the northern part of the Abiz fault where the rupture started (Figure 19). In the second test, we investigate if S1 and S2 source could caused a higher positive Coulomb stress changes on the first sub-event receiver fault plane than on the average rupture plane. We calculate the stress change at a depth of 9 km because it is the depth of this sub-event hypocenter (Berberian et al., 1999). Figure 23 represents the result, and show that this first sub-event is loaded by S1 and S2. The Coulomb stress change ranges from 0.02 to 0.8 bars around the northern part of the rupture, more than when when we take the average rupture into account. This calculation is more accurate because we modelled more precisely the receiver fault. From this second test, we confirm that the northern part of the Abiz fault has accumulated some stresses from the 1968 and 1979 earthquake. Considering that the 1997 Zirkuh rupture may have started in the north (Berberain et al., 1999), we suggest that the 1968 and 1979 earthquakes advanced the time of occurrence of the Zirkuh earthquake on the Abiz fault.

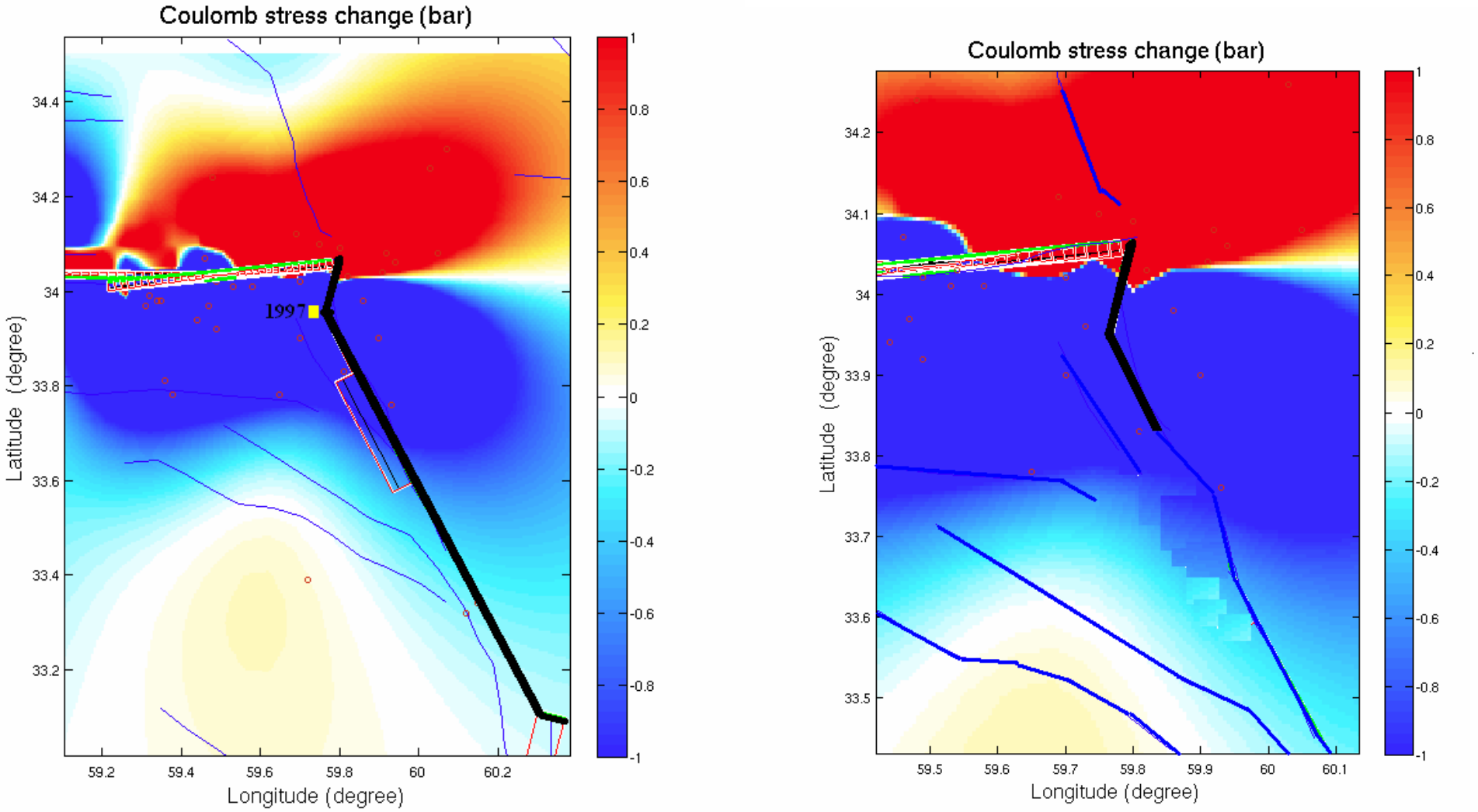

Figure 23: left panel: coulomb stress changes from the 1968 Aug 31 earthquake and 1979 Nov 27 (see table 4 and 5) at depth of 10 km on right-lateral strike slip fault oriented 156°N represented of the Abiz fault system on which rupture plane of 1997 May 10 occurred. The background colour scale is bar. 1968 and 1979 rupture plane is represented with the green line, the 1979 aftershocks up to 1997 mainshock represented by red circle. Right panel: coulomb stress changes from the 1968 Aug 31 earthquake and 1979 Nov 27 (see table II.1 and II.2) at depth of 9 km on right-lateral strike slip fault oriented 170°N represented of the north part of Abiz fault system on which first sub-event of 1997 May 10 occurred. The background colour scale is bar. 1968 and 1979 rupture plane is represented with the green line, the 1979 aftershocks up to 1997 mainshock represented by red circle.

4.4.3 Effects of 1979 Nov 27 and 1997 May 10 earthquakes on the distribution of aftershocks

- **Aftershocks of the 1979 Nov 27 earthquake**

In 1979, 48 Earthquakes occurred in the studied area, 22 before the E-Dasht-e-Bayaz earthquake and 25 earthquakes after the main shock. In 1978, only 2 earthquakes happened. We wonder if the increase of seismicity just before the 1979 Nov 27 announced the occurrence of the 7.1 earthquake. We can not assess this question because we do not have enough information on these foreshock events. Nevertheless, we can examine if the Coulomb stress change pattern calculated with S1 plus S2 sources on optimally-oriented fault system as receiver plane can explain the distribution of aftershocks just after 27th of November earthquake, and the seismicity to this main shock up to next main shock (1997 May 10). Figure 24 represents this result that the seismicity distribution is consistent with the Coulomb stress changes pattern. Indeed, most of the aftershocks localized in the lobs where the

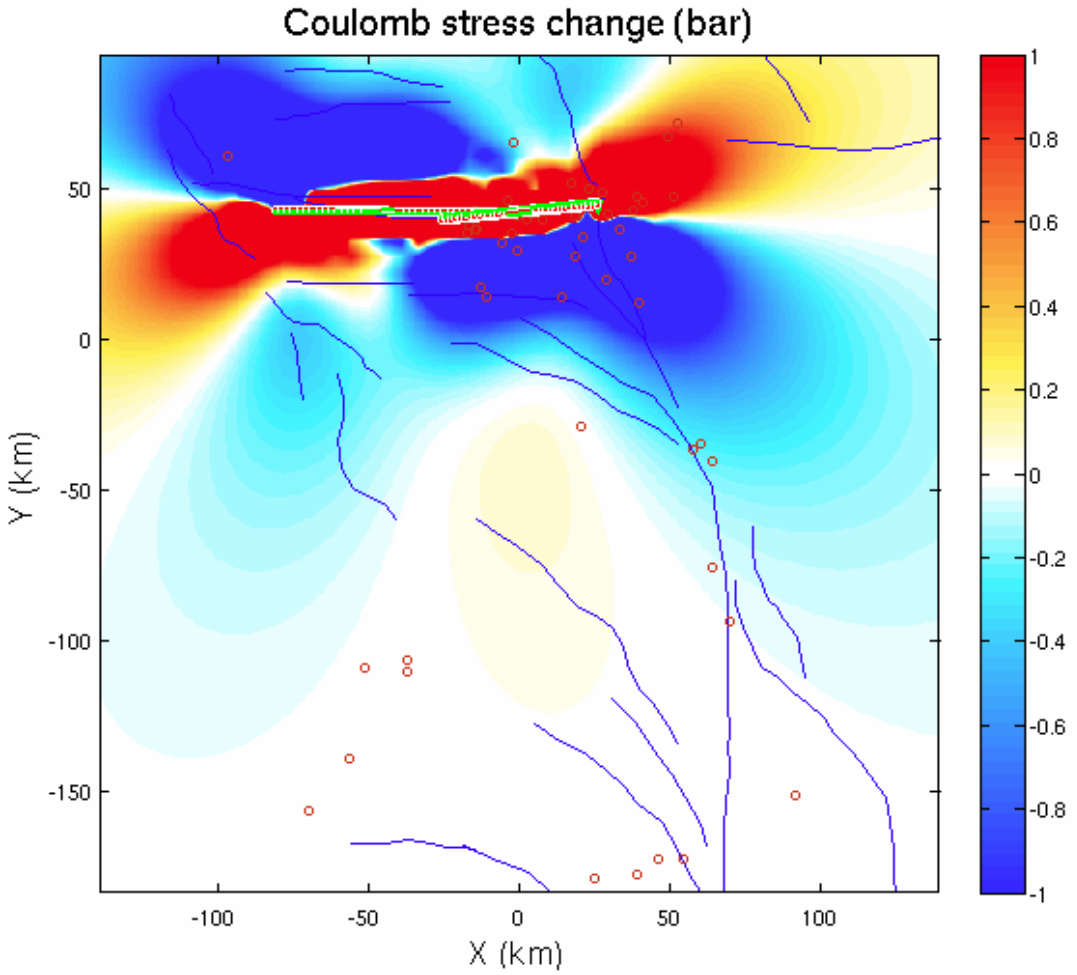

Figure 24: Coulomb stress changes from the 1968 Aug 31 earthquake and 1979 Nov 27 (Table 4 and 5) at depth of 7.5 km on optimally oriented fault system. The background colour scale is bar. 1968 and 1979 rupture plane is represented with the green line, the 1979 aftershocks and all earthquakes up to 1997 main shock represented by red circle.

Coulomb stress change is increased.

- **Aftershocks of the 1997 May 10 earthquake**

We investigate the effect of 1997 May 10 earthquake on its 3 principal aftershocks. We model the S3 source with the complex rupture determined in section 4.2.3 (5 segments of different strike, dip, slip and mechanism, summarized in Table 7). Figure 25 (left panel) presents the Coulomb stress change due to the S3 source on the first principal aftershock (16th of June) as receiver plane (120°N, 20° dip, thrust mechanism) at a depth of 10km (Table 7). It shows that the aftershock (black star) is located in a positive patch (1.9 bars). We notice that the mechanism of this aftershock is the same as the 4th sub-event of the main shock. Reproducing the calculation with the 4th sub-event as source, the Coulomb stress change at the location of the aftershock increased up to 2 bars. We conclude that it valids a strong relationship between the main shock and this aftershock with respect to the Coulomb stress hypothesis. This patch of positive Coulomb stress change is consistent with the high distribution of earthquakes in this area after the main shock (Figure 25, left panel).

Then we examine the influence of 1997 May 10 earthquake on the 2nd aftershock, that occurred on 20th of June on the southern part of the Abiz fault (Figure 19). We used the same source S3 as before, and calculated the stress transfer at 8 km depth on a rupture plane with a right lateral strike-slip mechanism oriented 188°N(Table 8), the Figure 25 (middle panel) presents the result and show that the 2nd aftershock lie in the strss shadow of 1997 main shock. The Coulomb change is -0.02 bars. The occurrence of this aftershock can not be explained by the Coulomb stress failure mechanism.

Finally, we examine the coulomb stress changes caused by the 1997 main shock on the 25th of June aftershock. The receiver plane has characteristic close to the 2nd aftershock: a right-lateral strike-slip mechanism and a 181°N orientation (Table 8). The calculation is made at 2km depth as supposed for the hypocenter of this aftershock. The result is presented on the right panel of Figure 25. Like the similar 20th of June aftershock, the 25th of June aftershock (black star) is located in the stress shadow of the 1997 main shock. The stress drops about -0.9 bars. The occurrence of this aftershock can not be explained by the Coulomb stress failure mechanism. In both case, it means that another process should explain the occurrence of these aftershocks about one month after the main shock. The chief candidate processes could be (1) the post-seismic stress transfer that amplify the amplitude of stress transfer and allow evolution of the spatial pattern of the stress transfer in time, and (2) the rate and stress-dependent friction that allow explaining the time dependence of aftershock occurrence in many case where static and post-seismic Coulomb stress hypothesis failed.

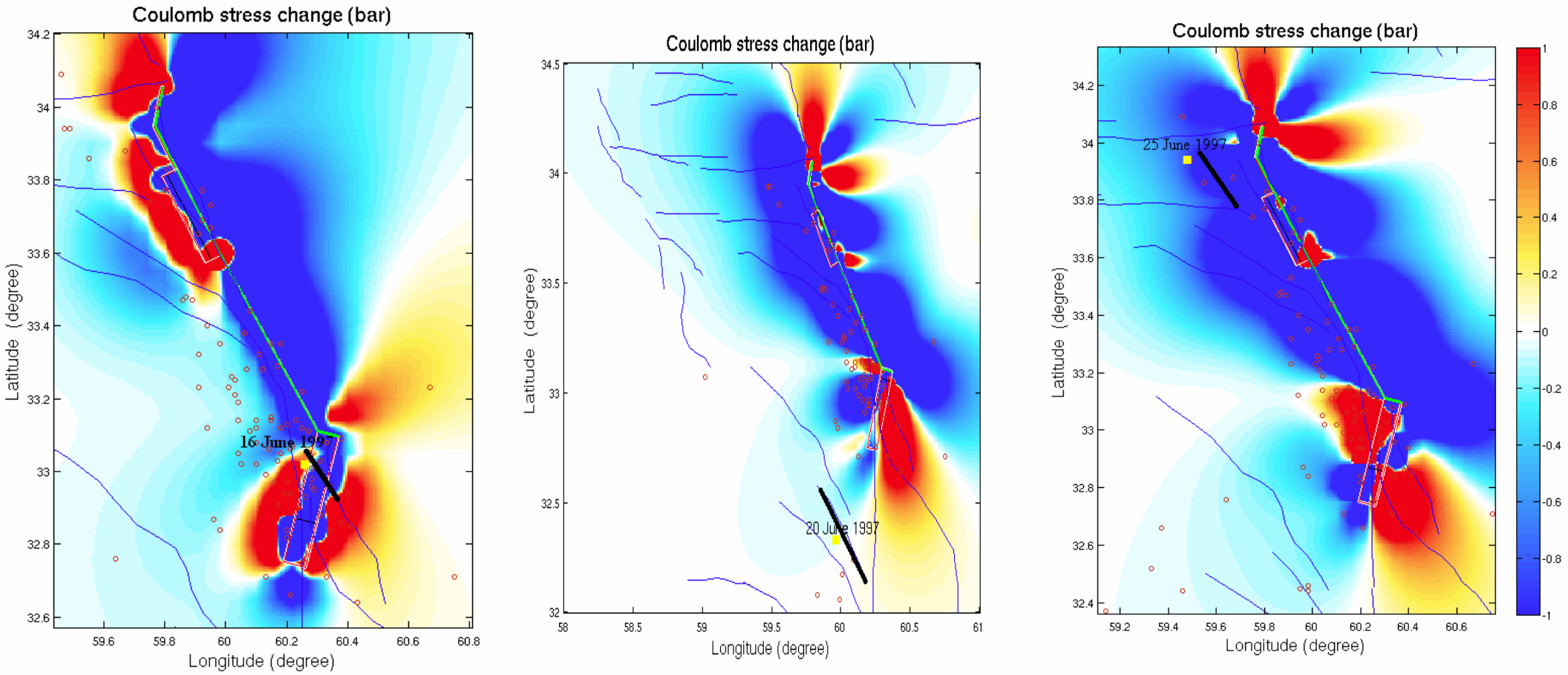

Figure 25: The Coulomb stress changes due to the 1997 May 10 with complex mechanism (Table 7) on: left panel: on the first aftershock (16th June 1997, see Table 8); Middle pane: on the 2nd aftershock (20th June 1997 , see table 4.5); Right panel: on the last aftershock (25th of June 1997, see table 45); The colour background is in bar, the 1997 rupture plane and aftershock rupture plane are represented by green line and black thick line, respectively. The seismic activity plotted by red circle since 1997 May 10 up to now, and main-shock of each aftershock represented by yellow rectangle. Active faults are represented by blue line.

4.4.4 Variation of the state of stress on the surrounding area due to the three major earthquakes

We examine first the relationship on the 3 large earthquakes and the distribution of the seismicity for the 1997-2007 period and secondly the effect of the 3 large earthquakes on the mapped fault in the area. For these calculations, we summed the effect of the three complex sources S1, S2 and S3 (Tables 4, 5, 7) to get the change of stress caused by the three earthquakes. We calculate the change of stress on optimally-oriented fault, with a strike-slip or a thrust mechanism. From the earthquake we studied, the orientation of fault, we assume that strike-slip and thrust are the principal mechanism of faulting in the area. . The results are represented on Figure 26. On the left panel, it shows the Coulomb stress change that result from the 3 major earthquakes on optimally-oriented strike-slip faults. On the right panel, it shows the Coulomb stress change that result from the 3 major earthquakes on optimally-oriented thrust faults. Most of the studied area lies in the stress shadow but all the end of faults or fault segments are loaded. These areas can experienced an increased of stress about 0.2-5 bars. In the strike-slip optimally-oriented case, the effect of the 1968, 1979 and 1997 events tend to positively accumulate whereas in the thrust optimally-oriented case the effect of the 1968 and 1979 and the effects of the 1997 event tend to negatively accumulate, in particular at the intersection of the two system. In both case, the south part of the Abiz fault is largely loaded. It is also a place of high production of earthquakes in the 1997-2007 periods. Except in this area, the distribution of the seismicity does not follow the stress pattern very well. We think that other processes should be tested to explain the whole distribution of seismicity in space and time. Finally, we use these calculations to infer which faults have their potential to fail increased due to the 3 large earthquakes. According to The calculation of the Coulomb stress change on optimally-oriented strike-slip faults (Figure 26, left panel) shows that the active fault A and B are positively affected by the 3 events. The calculation of Coulomb stress change on optimally-oriented thrust fault shows that some faults, fault C, fault D and most part of fault F, are positively affected by the 3 large earthquakes. We suggest to carefully surveying these A, B, C, D and F faults using geodetic and seismologic measurements. According to our study, the probability that an earthquake occurs on these fault is higher than on the other faults of the area.

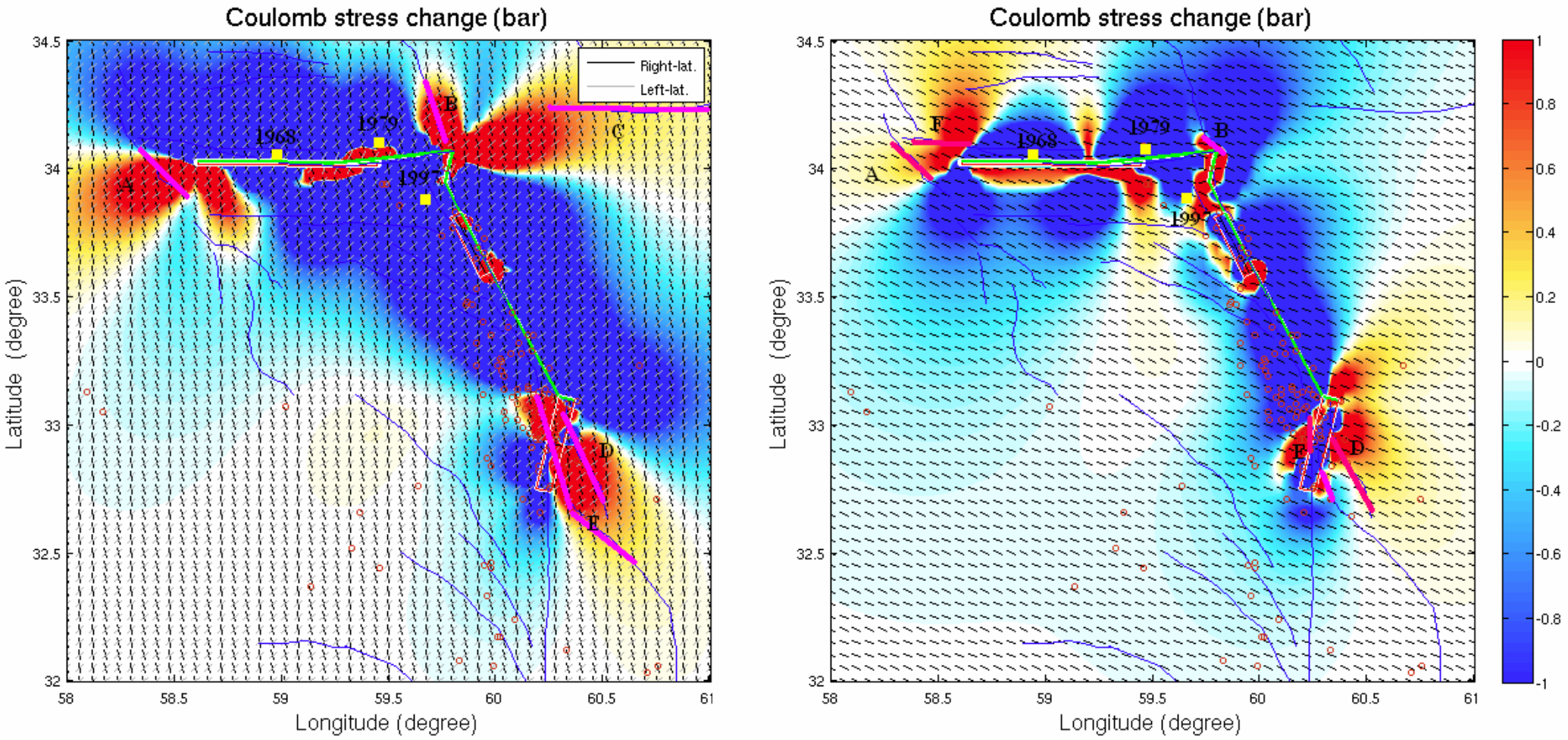

Figure 26 The Coulomb stress changes caused by the three major earthquakes on optimally-oriented strike slip(left panel) ; on optimally-oriented thrust faults. The background colour scale is in bar, the source planes are represented by green lines, the seismicty from 1997 May 10 up to now be shown by red circle. The active faults represented by blue line. The potential active faults represented by pink thick line (A, B, C, D, E, F). Main-shocks represented by yellow rectangles.

5 Conclusion

In this study, we obtained the following major results of the GPS analysis:

(1) The first significant results of IPGN will be achieved after 2 years of operation, according to comparison with close by campaign data.

(2) We realized that the combination of campaign data with continuous data from the permanent network can improve the results of the campaign network.

(3) The regional network solution combined with global IGS stations is the best strategy for stabilizing the time series of Iranian permanent GPS stations. Thanks to this noise reduction tectonical signals will be easier to identify in the individual time series.

(4) The more precise analysis of the atmosphere using VMF1 and ATML improves significantly the estimation of the height components.

(5) The age of the permanent stations (at least 2 years) and the interval covered by campaigns on temporary stations (at least 4 years) are the most important criteria for obtaining significant results (at the level of 2 mm/yr).

(6) The time-series analysis is a rapid method to observe some large non-tectonical phenomena in particular regions such as TOUS and NISH stations with strong periodical subsidence.

According to this study, duo to age of permanent network on most region which is covered whole Iran, in particular on the NE and E area. We are not able to interperet from tectonically approach and it needs to continue at least more than tow years processing on all stations covered on that regions.

We study the stress interaction between faults in the Dasht-e-Bayaz and Abiz fault systems area. We show clearly; (1) that the 1968 earthquake could trigger the 1979 main shock earthquake, (2) that the 1968 and 1979 earthquakes could trigger the aftershocks of 1979 Nov 27, and (3) that the 1968 and 1979 earthquakes could trigger the 1997 earthquake. For the latter, we show that most of the rupture of the May 10 1997 lies in the stress shadow generated by the 1968 and the 1979 earthquakes. Nevertheless, the northern part of the rupture undergoes a static stress change of +0.8 bar. This is sufficient to trigger the first sub-event of this complex large event and then the total rupture. We also compared the distribution of the seismicity since 1997 and the location of known active faults with respect to the influence of the three large earthquakes on the state of stress. We show that the distribution of earthquakes after 1997 is high on positive lob in which Coulomb stress rise, despite there are considerable number of earthquakes on the stress shadow. We also suspect that few faults have their potential to fail increase. These faults are located in the south part of Abiz fault, North East part of Abiz fault and in the Dasht-e-Bayaz fault area (A, B, C, D, F active faults, Figure 26). Based on these results, we suggest continuing this study in combining tectonic results and modelling results. For example, it would be interesting to better know the mechanism of the faults already mapped from satellite images as well as their recurrence time, in particular the ones we point out in this study. Moreover, if we calculate the tectonic stress rate in the area from the GPS data and if we could have access to the recurrence time of the 3 large earthquakes, we could investigate how much time each past earthquake advance the next one. Finally, we strongly suggest surveying carefully the faults we pointed out using geodetic and seismologic measurements.

6 Reference

Ambraseys, N.N. & Melville, C.P., 2005. A History of Persian Earthquakes, New edition, Cambridge University Press, New York.

Ambraseys, N.N. & Tchalenko, J.S., 1969. Dasht-e-Bayaz Earthquake of 31 August 1968, UNESCO, Publ. no. 1214/BMS, Paris.

Ambrasesys, N., Bilham, R., 2003, Earthquake and associated Deformation in Northern Baluchistan 1892-2001, Bul. Seis. Soc. Am, 93, 4, 1537-1605.

Altammi, Z., Sillard, P., Boucher, C., 2002, ITRF2000: a new release of the International Terresterial Reference Frame for earth science applications, J.geophys. Res., 107(B10), 119-137.

Berberian, M., J. A. Jackson, M. Qorashi, M. M. Khatib, K. Priestley, M. Talebian, and M. Ghafuri-Ashtiani (1999), The 1997 May 10 Zirkuh (Qa'enat) earthquake (Mw 7.2): Faulting along the Sistan suture zone of eastern Iran, Geophys. J. Int., 136, 671 – 694.

Berberian, M., 1979a. Evaluation of instrumental and relocated epicentres of Iranian earthquakes, Geophys. J. R. astr. Soc., 58,625-630.

Berberian, M. & Yeats, R.S., 1998. Patterns of historical earthquake ruptures in the Iranian Plateau, Bull. seism. Soc. Am.,in press.

Berberian, M. & Tchalenko, J.S., 1975. Dasht-e-Bayaz fault, Iran: earthquake and related structures in bedrock, Geol. Soc. Am. Bull.,86, 703-709.

Boehm, J., A. E. Niell, P. Tregoning, H. Schuh, 2006. The GMF: A new empirical mapping function based on numerical weather model data, Geophys. Res. Lett.,33(7), doi:10.1029/2005GL025546.

Boehm, J., Schuh, H., 2004, Vienna Mapping Function in VLBI analysis, Geophys. Res. 31, L01603, doi: 10.1029/2003GL018984.

Chu, D. & Godon, R.G., 1998, Current plate motions across the Red See, Geophys. J. IN., 135, 313-328.

DeMets, C., Gordon, R.G., Rrgus, D.F., Stein, S., 1994, Effect of recent revisions to the geomagnetic reversal time scale on estimates of current palte motions, Geophys. Res. Lett., 21, 2191-2194

Engdahl, E., Jackson, J., Myers, C., Bergman, E., Priestley, K., 2006, Relocation and assessment of seismicity in the Iran region, Geophys. J. Int. 167, 761-778.

England, P.C. & Molnar, P., 1990. Right-lateral shear and rotation as the explanation for strike-slip faulting in eastern Tibet, Nature, 344,140-142.

Haghipour, A. & Amadi,M., 1980. The November 14 to December 25,1979, Ghaenat earthquakes of northeast Iran and their tectonic implications, Bull. Seism. Soc. Am., 70, 1751-1757.

Heidbach, O., Fuchs, K., Müller, B., Reinecker, J., Sperner, B., Tingay, M., Wenzel, F., 2007, World stress map, WSM Release 2005, http://www.world-stress-map.org

Hessami, K., Jamali, F., Tabassi, H., 2003, Major active faults of Iran, seismotectonic dept. Seismology research center, IIEES

Herring, T. A., King, R. W., McClusky, S. C., 2007, Reference Manual Global Kalman filter VLBI and GPS analysis program. Release 10.32, Department of Earth, Atmospheric, and Planetary Sciences Massachusetts Institute of Technology.

Herring, T. A., King, R. W., McClusky, S. C., 2007, GAMIT Reference Manual GPS analysis at MIT. Release 10.32, Department of Earth, Atmospheric, and Planetary Sciences Massachusetts Institute of Technology.

Jadidi, A., Walpersdorf, A., Nankali, H., Aghamohamadi, A., Tavakoli, F., Djamur, Y., 2006, Sterategy of Iranaian Permanent GPS Network, Geomatics 85 Conference (NCC) Iran.

Jackson, J.A., Haines, A.J. & Holt,W.E., 1995. The accommodation of Arabia-Eurasia plate convergence in Iran, J. geophys. Res., 100,15 205-15 219.

Jestin, F., Huchon, P., Gauliers, J.M, 1994, The Somalia plate and the east African Rift system: present-day kinematics, Geophys. J. Int., 116, 637-654.

Kanamori, H. & Anderson, D.L., 1975. Theoretical basis of some empirical relations in seismology, Bull. seism. Soc. Am., 65, 1073–1095.

King, G.C.P., Stein, R.S. & Lin, J., 1994. Static stress changes and the triggering of earthquakes, Bull. seism. Soc. Am., 84, 935-953.

King, Geoffrey C. P. and David D. Bowman, 2003, The evolution of regional seismicity between large earthquakes, J.Geophys. Res. , 108, NO. B2, 2096,doi:10.1029/2001JB000783

Manighetti ‘s cartography (pers. comm., 2007) corresponding to a detailed surface rupture map focused on the studied area and derived from satellite images (Landsat) and precise MNT

Manighetti’s earthquake catalogue (pers. comm., 2007) corresponding to a synthesis of the Engdhal and Ambaraseys and Melvile, 2005 earthquake catalogues.

Masson, F., Chery, J., Hatzfeld, D., Martinod, Vernant, P., Tavakoli, F., and Ghafory-Ashtiani, M., 2005, Seismic versus asesimic deformation in Iran inferred from earthquakes and geodetic data. Geophys. J. Int., 160, 217-226.

Meyer, B., and K. Le Dortz, 2007, Strike-slip kinematics in Central and Eastern Iran: Estimating fault slip-rates averaged over the Holocene, Am.G.U, Tectonics, 26, TC5009, doi:10.1029/2006TC002073.

Niazi, M., Kanamori, H., 1981, Source parameters of 1978 and 1979 Qainat, Iran, earthquakes from long-period surface waves; Bul. Seis. Soc. Am, 71, 4, 1201-1213.

Okada, Y., 1992. Internal deformation due to shear and tensile faults in a half-space, Bill. seism. Soc. Amer., 82, 1018–1040.

Stein, R.S., 1999. The role of stress transfer in earthquake occurrence, Nature, 402, 605–609.

Stein, R.S., Barka, A.A. & Dieterich, J.H., 1997. Progressive failure on the North Anatolian fault since 1939 by earthquake stress triggering, Geophys. J. Int., 128, 594–604.

Tatar, M., Hatzfeld, D., Martinod, J., Walpersdorf, A., Ghafouri-Ashtiani, M, Chery, J., 2002, The present-day deformation of the central Zagros from GPS measurements, Geophys. Res. Lett., 29, 1927-1930.

Tavakoli. F., 2007, Déformation actuelle et cinématique des actives dans le Zagros et l'E iranien, PhD thesis.

Tchalenko, J. & Ambraseys, N. 1970. Structural analysis of the Dasht-e-Bayaz earthquake fractures, Geol. Soc. Am. Bull., 81, 41-60.

Toda, S., Stein, R., Lin, J., Sevilgen, V., 2007, user guide of Coulomb 3.0 Software, Graphic-rich deformation and stress-changes software for earthquake, tectonic, and volcano research &nd teaching: http://www.coulombstress.org

Toda, S., Stein, R., Richards-Dinger, K. & Bozkurt, S., 2005. Forecasting the evolution of seismicity in southern California: Animations built on earthquake stress transfer, J. geophys. Res., 110, B05S16, doi:10.1029/2004JB003415.

Toda, S. & Stein, R.S., 2002. Response of the San Andreas fault to the 1983 Coalinga-Nunez earthquakes: An application of interaction based probabilities for Parkfield, J. geophys. Res., 107(B6), 2126, doi:10.1029/2001JB000172.

Tregoning, P. and T. van Dam, 2005, The effects of atmospheric pressure loading and 7-parameter transformations on estimates of geocenter motion and station heights from space-geodetic observations. J. Geophys. Res., 110, B03408, dio:10.1029/2004JB003334, 2005.

Tregoning, P. and T. van Dam, Atmospheric pressure loading corrections applied to GPS data at the observation level, Geophys. Res. Lett., 32, L22310, doi:10.1029/2005GL024104, 2005.

US Geological Survey: http://earthquake.usgs.gov

Vernant, Ph., F. Nilforoushan, D. Hatzfeld, M. R. Abassi, C.Vigny, F. Masson, H. Nankali, J.Martinod, A. Ashtiani, R. Bayer, F. Tavakoli, and J. Chery , 2004, Present-day crustal deformation and plate kinematics in the Middle East constrained by GPS measurements in Iran and Northern Oman, Geophys.J.Int., 157, 381 – 398.

Walker, R., and J. Jackson , 2004, Tectonics of Central and Eastern Iran, Tectonics, 23, TC5010, doi:10.1029/2003TC001529.

Walker, B, J. Jackson, C. Baker, 2004, Active faulting and seismicity of the Dasht-e-Bayaz region, eastern Iran, Geophys. J. Int. 157, 265-282.

Zeng, Y.H., 2001. Viscoelastic stress-triggering of the 1999 Hector Mine earthquake by the 1992 Landers earthquake, Geophys. Res. Lett., 28, 3007–3010.

Zhang, J., Bock, Y., Johnson, H., Fang, P., Williams, S., Genrich, J., Wdowinsky, S., Behr, J., 1997, Southern California Permanent GPS Geodetic Array: Error analysis of daily position estimates and site velocities, J.geophys. Res., 102,18 035-18 055.